

MASARYKOVA UNIVERZITA
PŘÍRODOVĚDECKÁ FAKULTA
ÚSTAV TEORETICKÉ FYZIKY A ASTROFYZIKY

Bakalářská práce

Brno 2018

Jaroslava Secká



MASARYKOVA UNIVERZITA

PŘÍRODOVĚDECKÁ FAKULTA

ÚSTAV TEORETICKÉ FYZIKY A ASTROFYZIKY



Určování výkonů jetů v obřích eliptických galaxiích

Bakalářská práce

Jaroslava Secká

Vedoucí práce: doc. Mgr. Norbert Werner, Ph.D.

Brno 2018

Bibliografický záznam

Autor: Jaroslava Secká
Přírodovědecká fakulta, Masarykova univerzita
Ústav teoretické fyziky a astrofyziky

Název práce: Určování výkonů jetů v obřích eliptických galaxiích

Studijní program: Fyzika

Obor: Astrofyzika

Vedoucí práce: doc. Mgr. Norbert Werner, Ph.D.

Akademický rok: 2017/2018

Počet stran: viii + 61

Klíčová slova: rentgenové záření, eliptická galaxie, rentgenová bublina, neuronová síť, NGC 4649

Bibliographic entry

Author: Jaroslava Secká
Faculty of Science, Masaryk University
Department of Theoretical Physics and
Astrophysics

Title of Thesis: Estimating jet powers in giant elliptical galaxies

Degree Programme: Physics

Field of study: Astrophysics

Supervisor: doc. Mgr. Norbert Werner, Ph.D.

Academic Year: 2017/2018

Number of Pages: viii + 61

Keywords: X-ray, elliptical galaxy, X-ray cavity,
neural network, NGC 4649

Abstrakt

V průběhu posledních několika dekád byly objeveny poklesy jasů v rentgenových pozorováních kup, skupin galaxií i eliptických galaxiích. Tyto poklesy jsou způsobeny jety centrální supermasivní černé díry, které odhrnují okolní horký difúzní plyn a vytváří v něm bubliny. Ze znalosti jejich velikosti a stáří lze odhadnout výkony jetů za předpokladu, že množství energie disipované ve formě šoků je zanedbatelné. Podle zjištění Allen et al. (2006) existuje korelace mezi Bondiho akrecí a výkonem jetů, naznačující existenci zpětné vazby mezi aktivním galaktickým jádrem a rentgenovým plynem hostující galaxie. Nicméně, protože neexistuje objektivní způsob detekce bublin a určení jejich velikostí, výkony jetů určené různými autory se mohou značně lišit a to i v případě, kdy vyjdou z totožných dat. To následně značně komplikuje studium fyzikální podstaty této zpětné vazby. Obsahem této práce je studium technik zpracování obrazu, které se používají na detekci bublin s vyšetřením rozličných zdrojů nejistot ovlivňující určené výkony. Následně je s cílem objektivizace celého procesu navrhnout nový způsob jejich detekce inspirovaný prací Fort (2017), který je zde poprvé aplikován na snímky skutečných galaxií - pomocí neuronové sítě.

Abstract

For the past couple of decades, surface brightness depressions in the X-ray emission of clusters, groups and elliptical galaxies have been discovered. They are believed to be created by the jets of the central supermassive black hole. As the jet propagates it pushes aside the hot X-ray emitting gas, creating voids. These are then observed as X-ray cavities. Since these ‘bubbles’ are inflated by the jets, their sizes can be used to estimate jet powers under the assumption that the energy dissipated in form of shocks is negligible in comparison. Plotting the Bondi accretion as a function of summed power of both jets shows a correlation between them (Allen et al., 2006), suggesting an existence of AGN (active galactic nuclei) feedback. However since there is no objective way of defining cavity sizes, values of the derived powers of the jets can differ by significant amount even when the same data are used by various authors, hindering our understanding of the underlying physics. In this work, traditional imaging techniques used for cavity detection are examined along with the identification of various sources of uncertainties. In a search for an objective way of defining cavity sizes, a novel method inspired by Fort (2017) is proposed and for the first time tried on images of real galaxies – a neural network.



MASARYKOVA UNIVERZITA
Přírodovědecká fakulta

ZADÁNÍ BAKALÁŘSKÉ PRÁCE

Akademický rok: 2017/2018

Ústav: Ústav teoretické fyziky a astrofyziky

Studentka: Jaroslava Secká

Program: Fyzika

Obor: Astrofyzika

Ředitel Ústavu teoretické fyziky a astrofyziky PŘF MU Vám ve smyslu Studijního a zkušebního řádu MU určuje bakalářskou práci s názvem:

Název práce: Určování výkonů jetů v obřích eliptických galaxiích

Název práce anglicky: Estimating jet powers in giant elliptical galaxies

Oficiální zadání:

AGN jet powers in giant elliptical galaxies surrounded by hot X-ray emitting halos can be inferred from the energies and time-scales required to inflate radio lobes, which displace the X-ray emitting gas, producing apparent cavities in X-ray images. The student will perform analysis of X-ray data for a sample of nearby X-ray bright giant elliptical galaxies to estimate the jet powers and the level of associated systematic uncertainties.

Jazyk závěrečné práce: angličtina

Vedoucí práce: doc. Mgr. Norbert Werner, Ph.D.

Datum zadání práce: 31. 10. 2017

V Brně dne: 20. 11. 2017

Souhlasím se zadáním (podpis, datum):


.....
Jaroslava Secká
studentka


.....
doc. Mgr. Norbert Werner, Ph.D.
vedoucí práce


.....
prof. Rikard von Unge, Ph.D.
ředitel Ústavu teoretické fyziky a
astrofyziky

Poděkování

First and foremost, I would like to offer my deepest gratitude to my supervisor doc. Mgr. Norbert Werner, Ph.D. for showing me the wonders of science, his encouraging and motivational nature and patience. Secondly, I am grateful to Mgr. Filip Hroch, Ph.D. for introducing me to limitless capabilities of python and pointing me in this area of research. My thanks also goes to my friend and colleague Antónia Vojteková, for creating and training the neural network with me and bearing with my unending questions and remarks. I am further thankful to countless others who selflessly offered their practical advice, witty insights and valuable data and without whom this work would not come into existence. And lastly, I am grateful for the wonderful opportunity to participate in training led by experts in X-ray astronomy in Netherlands Institute for Space Research SRON as well as the AHEAD High Resolution X-ray Astronomy School via funding of AHEAD Trans-National Access.

Prohlášení

Prohlašuji, že jsem svoji bakalářskou práci vypracovala samostatně s využitím informačních zdrojů, které jsou v práci citovány.

Brno 9. května 2018

Podpis autora

Contents

Introduction	1
1 Elliptical galaxies and Active Galactic Nuclei	2
1.1 Basic properties of elliptical galaxies	2
1.2 The Interstellar Medium	3
1.3 AGN feedback loop	3
1.4 Cavities – their formation and properties	4
1.4.1 Observed properties and correlations	4
1.4.2 Cavity shapes and orientation	5
1.4.3 Estimating the ages of cavities	6
1.4.4 Cavity stability	7
1.4.5 Enthalpy of the cavities	8
1.4.6 Power of the jets	9
2 X-ray data processing	11
2.1 Chandra and ACIS	11
2.2 Backgrounds and foregrounds	12
2.2.1 Instrumental backgrounds	12
2.2.2 Cosmic backgrounds	12
2.3 Observations and data reduction	13
2.3.1 Imaging techniques	13
2.3.2 Extraction of the spectra	13
2.3.3 Spectral data analysis	15
3 Cavity detection	16
3.1 Traditional imaging techniques	16
3.1.1 Unsharp masking	16
3.1.2 Beta modeling	17
3.1.3 Gaussian Gradient Magnitude filter	17
3.2 Novel methods based on Neural Networks	18

3.2.1	Introduction	18
3.2.2	The Network Architecture	20
3.2.3	Creation of the dataset	20
3.3	Computation of uncertainties	22
4	Results	23
4.1	Detailed study of NGC 4649 (M60)	23
4.1.1	Radial profiles	23
4.1.2	Cavity detection	25
4.2	Application to other galaxies	29
4.2.1	NGC 4472 (M49)	30
4.2.2	M84 (NGC 4374)	33
4.2.3	NGC 5044	36
4.2.4	NGC 5813	39
4.2.5	NGC 708 (A262)	43
5	Discussion	46
5.1	Imaging techniques and their influence on derived cavity volumes	46
5.2	Systematic uncertainties associated with the deprojected profiles	48
5.2.1	Anti-correlation of metallicity and normalization	48
5.2.2	Choice of the fitting range	50
5.3	Power of the jets	51
5.4	The use of neural networks for cavity detection	54
	Conclusions and future outlook	56
	Bibliography	57

Introduction

For the past couple of decades, surface brightness depressions in the X-ray emission of clusters, groups and elliptical galaxies have been discovered. They are believed to be created by the jets of the central supermassive black hole. As the jet propagates it pushes aside the hot X-ray emitting gas, creating voids. These are then observed as cavities or bubbles.

Since these bubbles are inflated by the jets, their sizes can be used to estimate jet powers under the assumption that the energy dissipated in form of shocks is negligible in comparison. Consequently, correlations between the jet powers and the accretion rate can be studied, explaining why the central gas is not cooling down even though it loses energy via X-ray radiation (see section 1.3).

However, no objective way of defining cavity sizes exist at present. As a result, depending on the technique used, various jet power can be inferred. Furthermore, various authors can find different jet powers even when the same data are used.

This work explores imaging techniques used for cavity detection as well as the possibility of employing neural network for the task in order to objectify the whole process. Various sources of uncertainties influencing the estimation of the jet powers are identified as well.

Chapter 1 briefly describes elliptical galaxies and introduces related key terms. Furthermore, it summarizes what is known about cavities based on observations and simulations. Chapter 2 gives an account of the Chandra satellite and its instrument which were used for obtaining presented data. Various sources of background contaminating the observations are discussed as well. Furthermore, the details of the data processing and employment of the techniques described in the next chapter are presented. Chapter 3 details the traditional imaging techniques used for cavity detection so far. Furthermore, it proposes the possibility of using neural networks for the task and summarizes the employed architecture along with explanations of relevant key terms. A brief description of the creation of the dataset used for training the network is presented as well. Following chapter 4 reports the obtained results which are interpreted and discussed in the final chapter 5.

Chapter 1

Elliptical galaxies and Active Galactic Nuclei

Nearby giant elliptical galaxies offer a unique window to study the interaction of Active Galactic Nuclei (AGN) and Interstellar Medium (ISM). Their low temperatures as compared to clusters are more easily measured with modern X-ray satellites and their AGNs can more easily disturb the surrounding diffuse gas due to their shallower gravitational potentials. In combination with their low redshifts, AGN feedback loop can be studied in great detail with hope of unraveling the underlying physics. (Werner et al., 2012; Randall et al., 2015)

This chapter introduces basic properties of elliptical galaxies, ISM, AGN feedback loop and mainly focuses on X-ray cavities and how can they help us to estimate the power of the jets produced by the supermassive black hole (SMBH).

1.1 Basic properties of elliptical galaxies

In the Hubble sequence, elliptical galaxies belong among early-type galaxies. They constitute about 20 % of all known galaxies and are found in denser environments than spirals, most commonly in galaxy clusters. Typical massive elliptical galaxy hosts a SMBH in its core with mass of $\sim 10^6 - 10^{10} M_{\odot}$. The SMBH evolve together with its hosting galaxy as is suggested by a tight correlation of its mass with the mass of the host galaxy. (Longair, 2011)

Furthermore, ellipticals are filled with X-ray emitting gas. However, most of their mass consists of a dark matter halo with the stellar component being dominant in the innermost parts. Additionally, they have negligible or no star-formation and thus are dominated by the old stellar population. This gives rise to them being referred to as 'red and dead'. They possess high masses and are of regular spheroidal shapes with low ellipticities which

generally do not exceed ~ 0.2 . Most of them are assumed to be close to hydrostatic equilibrium although Diehl and Statler (2007) argue that since no correlation between shape of the stellar distribution and hot gas morphology exists, the gas in the core has to be disturbed at least to a degree where the information about the shape of the underlying gravitational potential is lost. That is most likely caused by the Active Galactic Nuclei which stir up the central gas.

Apart from ISM, low mass X-ray binaries constitute a notable source of X-ray radiation in elliptical galaxies.

1.2 The Interstellar Medium

Elliptical galaxies are filled with hot diffuse gas extending far beyond the stellar population. The gas was in this work termed as ISM. It is an optically thin, highly ionized plasma in collisional ionization equilibrium. Due to its high temperature $\sim 10^6 - 10^7$ K it emits X-ray radiation (Longair, 2011). Its density is so low, that if you were to exhale on a cold day and spread the amount of visible vapour over a cube with each side one kilometer long, you would get a density about a thousand to a million times greater than the ISM density (Schlegel, 2002).

The ISM emission is dominated by thermal bremsstrahlung. Its emissivity spectrum is flat up to frequencies $hf \sim kT$, beyond which it has an exponential cut-off (Longair, 2011). Based on the metallicity¹ of the gas, various emission lines are visible as well, mainly those of helium-like elements. The main source of ISM chemical enrichment are supernovae and stellar winds.

1.3 AGN feedback loop

Since the ISM radiates in X-rays, it losses energy proportional to the square of its density. As a result, the denser regions in the core would be expected to cool down at much shorter times (~ 0.1 Gyr) than their ages. Consequently, the cool gas would accrete and young stars would form. However, even though star formation is sometimes observed, it is at levels far below those expected. The elliptical galaxies are mostly ‘red and dead’.

In order to explain this, a self-regulated AGN feedback loop was proposed. Number of observational proofs exist which support this theory. Among the most profound ones belong cavities, shock fronts and cool filaments near central radio sources. (McNamara and Nulsen, 2012)

The basic principle of the AGN feedback loop goes as follows. If we take a simple spherically symmetric accretion model called Bondi accretion, for $\gamma = 5/3$ gas, it depends on gas properties only through entropy as $\sim s^{-3/2}$ where entropy is defined as $s = k_B T \cdot n_e^{-2/3}$. This implies that when the AGN heating causes the gas near the core to expand and thus effectively lowers its density, the accretion rate lowers as well. However, as the gas radiates away its energy, it contracts and compresses itself, causing the accretion rate

¹In astrophysics, all elements heavier than Helium are called metals.

to rise again. This consequently leads to an increase of the power of the jets which is proportional to the entropy and the cycle repeats. (McNamara and Nulsen, 2007)

Supporting the notion of the self-regulated feedback loop rather than a simple AGN heating is a strong correlation between cavity power and X-ray luminosity of the ISM within the cooling radius (see fig. 8 in McNamara and Nulsen (2007)). This suggests that the AGN ‘knows’ about the cooling gas and balances its output to prevent star formation. Furthermore, their results also show that nearly all clusters with strong cooling flows harbour powerful cavity systems. Moreover, the AGN feedback is operating at centres of cooling atmospheres spanning seven orders of magnitude in terms of X-ray luminosity between $\sim 10^{38}$ and 10^{45} erg s⁻¹. This excludes other heating processes as the main agents, since thermal conduction and dynamical friction are unimportant in the atmospheres of groups and ellipticals. However, how is the energy from AGN distributed throughout the gas is still not well understood. (McNamara and Nulsen, 2012)

1.4 Cavities – their formation and properties

Massive elliptical galaxies host powerful engines in their cores called AGN. A pair of opposing jets is emitted from the central AGN, composed of relativistic particles that push aside the surrounding hot X-ray emitting gas and create pockets observed as surface brightness depressions called cavities or bubbles. Since they are filled with relativistic particles, they are often bright in radio. From their sizes, the energy required to inflate them can be determined. This allows us to estimate the powers of the jets which created them. The following paragraphs describe the details of this calculation, the assumed approximations as well as further information that can be learned from the study of cavities.

1.4.1 Observed properties and correlations

Finding and defining cavities objectively is a complex issue which remains to be solved. Nevertheless, several systematical studies for their search have been conducted, most notably by Shin et al. (2016), Dong et al. (2010) and Birzan et al. (2004). These works have uncovered new or confirmed existence of previously suggested properties of the cavities in relation to their host galaxies.

One of the most striking observed property is a strong correlation between the semi major axis of a cavity and its distance from the central SMBH. While not surprising as an intrinsic property curious is that this relation holds well even though projected dimensions are studied. This suggests that projection effects are not of great importance and also that ellipticity of most of the cavities is rather low. Encouraging is also the fact, that the relations found by Shin et al. (2016), Dong et al. (2010) and Birzan et al. (2004) agree within 1σ uncertainties even though somewhat subjective ways of defining cavity sizes were used by various authors.

Additionally, according to Shin et al. (2016), no strong dependence appears to exist to

tie the cavity sizes to their environment.² Many objects with the same gas temperatures display multiple cavities of various sizes. No strong correlation between the 1.4 GHz radio luminosity and a cavity detection rate appears to exist either (Dong et al., 2010).

The detection rate of cavities declines for less massive systems, suggesting that the number of cavities is a function of galaxy density. However, this finding is strongly influenced by selection effects, since larger systems usually have larger cavities which are easier to detect. Shin et al. (2016) also note, that larger cavities are on average detected at higher redshift. However, detection of small cavities at high redshift is beyond the resolution limit of Chandra.

Moreover, most of the targets studied by Shin et al. (2016) whose sample covered large dynamical range from clusters to individual galaxies have more than two cavities, implying multiple AGN outbursts. However, Dong et al. (2010) studying galaxy groups did not find any system which would have more than two cavities. However, this might be a result of insufficient number of counts, making the detection of more distant cavities impossible.

Furthermore, the cavities show a trend in terms of orientation as is further expanded upon in the following section 1.4.2. Most of the found cavities have the semi major axis oriented either along the direction of the jet or perpendicular to it (see fig. 12 in Shin et al. (2016)). However, since the cavity shapes were determined based on visual inspection, the uncertainty of this result is rather large.

To conclude, a clear correlation between the cavity size and its distance from the core on large dynamical scale exists. On the other hand, cavity sizes seem to be uninfluenced by their environment, suggesting that their formation and evolution is more dependent on the AGN and central gas density. Their detection rate seems to decline for less massive systems. Most commonly, galaxies display one generation of cavities or none although systems with more generations of cavities are known as well. Most of the cavities are oriented either along the jet axis or perpendicular to it.

1.4.2 Cavity shapes and orientation

The shapes of the cavities are generally assumed to be close to prolate ellipsoids with the main axis along the direction of the jet and the minor one perpendicular to it (this holds true e.g. for most of the cavities in Shin et al. (2016)). Sometimes, as an upper limit of the volume, an oblate shape is considered. However, the observed cavities do not always seem to be describable by such a simple geometry, since their apparent shapes also depend on the projection effects. Furthermore, the radio lobe emission is not always symmetrical for both of the jets. In this section, the presumed shapes of cavities based on simulations are described along with the influence of projection effects on them.

In order to determine the enthalpy of a cavity, apart from the pressure of the surrounding ISM, it is customary to take into account only the volume of the bubble as the main criterion by which the amount of energy deposited in it is judged. However, Guo (2015) states that the shape of the cavity is of great importance as well. Most of the observed young cavities tend to be elongated either radially or in the direction perpendicular to it. This

²Panagoulia et al. (2014) also reported no dependence of the cavities on temperature of the surrounding diffuse gas for a sample consisting of groups and clusters.

is commonly interpreted as to depend only on whether the jet giving rise to the bubble propagates supersonically or subsonically. However, depending on the jet composition this need not to be the case. Even supersonic jets can produce radially elongated bubbles providing they are light enough.

Generally, the radial elongation increases with jet density, velocity and duration. On the other hand, it decreases with jet energy density and radius. In order to disentangle the effects of these parameters, the shapes of the cavities could be used, specifically their ‘top wideness’. Depending on whether the cavities are wider closer to the core or at the opposite end they can be described as bottom or top wide. Very light, internally subsonic jets produce bottom-wide cavities whereas top-wide cavities are produced by heavier jets with internally supersonic velocities. Nevertheless, bottom-wide cavities can be also produced by very light jets with long duration. Furthermore, based on simulation in Brügggen et al. (2009), the bubbles tend to expand more rapidly in the direction perpendicular to the radial one while sometimes even being compressed in the radial one further changing the cavity shapes as they age. This holds true even for young cavities since none of the bubbles simulated by Brügggen et al. (2009) detached during the entire duration of the simulation.

In conclusion, if the shapes of the cavities could be determined more accurately, tighter constraints could be placed at the jet properties as well as the choice of the appropriate timescale for the cavity age estimation. However the shapes discussed so forth are the intrinsic ones. In real observations, it is probable that the cavities appear more circular due to projection effects (Birzan et al., 2004). Furthermore, gas sloshing may bend or rotate the radio lobes and X-ray cavities (Guo, 2015).³ In some cases, it even might be possible that the bending of cavities is a result of SMBH precession, as was suggested by Randall et al. (2011) for NGC 5813. As a result, it is unlikely that the top wideness of the cavities could be determined in real observations, especially also because the inclination of the studied galaxies is unknown. Although based on simulations in Brügggen et al. (2009) it was suggested that most of the observed systems have the jet axis at angles between 45° to 90° with the line of sight. However, the effect of inclination on the cavity shapes cannot be clearly disentangled from the effects caused by various jet properties in real observations at present.

1.4.3 Estimating the ages of cavities

In Birzan et al. (2004), three different time scales for cavity ages depending on the speed at which the bubbles rise were considered. The ages are calculated as $t = R/v$ where R is the projected distance of the middle of the cavity from the SMBH and v is speed at which the cavity rises.

Firstly, the sound of speed as the speed at which the bubble rises was considered. It is defined as $c_s = \sqrt{\gamma kT / \mu m_H}$ where $\gamma = 5/3$ and $\mu = 0.62$. Secondly, the buoyant rise timescale is often used. In this scenario the bubble rises buoyantly at terminal velocity $v_t = \sqrt{2gV/SC}$ where V is volume of the cavity, S is the cross section of the bubble and $C = 0.75$ is the drag coefficient. The gravitational acceleration is calculated from

³This is especially problematic if a radially symmetric model is subtracted for cavity size estimation as is often done.

stellar velocity dispersion under the approximation that the galaxy is an isothermal sphere as $g = 2\sigma^2/R$. Last but not least is the time required to refill the displaced volume $t_r \sim 2R\sqrt{r/GM(R)} = 2\sqrt{r/g}$ where r is the radius of the cavities (for ellipsoidal cavities $r = \sqrt{ab}$).

In this work, the sound speed timescale was used since only systems with young cavities are studied. The sound speed timescale is favored for jets with higher momentum and thus is usually used for younger cavities (Dunn et al., 2010). Young cavities close to the core are most likely still attached to the jet and thus they have significantly higher speeds than the buoyant timescale. The bubbles are presumed to rise buoyantly only after they detach from the core. The refill timescale seems least suited for the age estimation since it most heavily depends on estimation of unknown variables.

However, if the bubbles are very young, their age can be notably smaller than the corresponding sound crossing time (as well as all the other considered timescales since generally $t_{cs} < t_{buoy} < t_r$). This can in turn lead to the overestimation of the age of the cavities and thus underestimation of the power of the jets. Nevertheless, in case the jets were moving substantially supersonically they would produce strong shocks which are not observed. In most cases, only weak shocks or none are seen. (McNamara and Nulsen, 2007) Thus it would seem that the use of the sound of speed for estimating the age of young cavities is justified.

In conclusion, it is probable that the cavity ages are overestimated since momentum from the jet is not taken into account by the sound speed approximation even though the studied bubbles are probably still attached. This in turn leads to underestimation of the power of the jets. However, in order to determine the cavity age with higher precision, more information about the jet composition and its initial momentum would be needed.

1.4.4 Cavity stability

Every cavity disruption is essentially deviation from an adiabatic model. Based on hydrodynamical simulations numerous instabilities ought to form as the bubble rises. The shear flow between the low density bubble and its higher density surrounding medium develops Kelvin-Helmholtz instabilities. From their inflation, the bubbles possess momentum and as their material is accelerated into surrounding gas, Rayleigh-Taylor instabilities form. The simulated cavities are disrupted and over time mixed into their surroundings and dissipate completely. However, most of the observed bubbles have highly regular shapes. Surprisingly, the bubbles were found to be stable and resistant to the formation of various instabilities, leaving them intact for timescales over an order of magnitude longer than it ought to take for the instabilities to form. (McNamara and Nulsen, 2007)

The stability of the bubbles can be explained if the ISM viscosity is higher than it was presumed. Simulations of Guo (2015) show, that while the ISM viscosity significantly affects the long term stability of the bubbles, it does not bear notable influence on their shape while they are young. On the other hand it could also be explained if the jets are in fact magnetically dominated. A buoyant cavity can entrain magnetic field from the surrounding gas and create magnetic field around itself (McNamara and Nulsen, 2007). However the strengths of the magnetic fields in the bubbles as well as the ISM viscosity are

mostly unknown. Subsequently, it is not clear which of these effects ensure the observed stability of the bubbles or whether it is the combination of both. Nevertheless, bubbles of hot underdense gas and magnetically dominated bubbles behave differently as they rise through the surrounding gas allowing them to be distinguished (Brüggen et al., 2009). Unfortunately, the length of their rise time does not allow for this to be directly observed.

1.4.5 Enthalpy of the cavities

The enthalpy of the cavity is calculated as enthalpy of an adiabatic bubble under the assumption that it is in pressure equilibrium with its surrounding. For relativistic gas with $\gamma = 4/3$ this gives $E = 4pV$. Furthermore, it is assumed that the bubble is small in comparison to its distance from the center. Otherwise the density of the gas surrounding it could change significantly (Birzan et al., 2004). Moreover, it is presumed that close to their origin, the bubbles are overpressured. Afterwards they expand to reach the pressure equilibrium as they rise through the ISM (Brüggen et al., 2009). Even though the bubbles studied here are young, they are old enough not to be considered significantly overpressured anymore.

But even with these assumptions, the enthalpies are not always easily determinable. It has been observed, for example in the Perseus Cluster, that larger bubbles can sometimes break up to smaller ones. Thus it might be questionable which bubbles correspond to the same outburst. Furthermore, since the bubbles are assumed to be produced by bipolar jets of equal strengths, it would be expected that the bubbles produced in single outburst would have the same enthalpies. However that does not appear to be true in numerous cases. Furthermore, the discrepancy between their sizes does not seem to be explainable by projection effects alone.

Moreover, Diehl et al. (2008) found an apparent correlation between the inferred enthalpy of a bubble and its distance from the core. However there does not appear to be any physical reason for this correlation to exist, suggesting that the common method of estimation of the enthalpy of the cavities is significantly flawed. The multicavity systems are most suited for determining whether this correlation is real or a result of natural scatter and other effects. If the power of the jet is assumed to be constant at timescales corresponding to at least several outbursts, the power inferred from bubbles from various generations (produced by different outbursts) ought to be the same. However, that is not the case in Hydra A where the correlation appears to hold (Wise et al., 2007). On the other hand, in NGC 5813, where three generations of bubbles were observed, the outburst energy found for the cavities from the second generation is comparable to that of the third generation (Randall et al., 2015). The energy of the first generation of bubbles is an order of magnitude lower but that can be explained if the outburst is currently ongoing. Thus it would seem that the correlation between pV and distance of the cavity from the center is not a real feature. Nevertheless, it seems to hold for a large number of objects. It is still puzzling and it is not clear, what does it suggest about the uncertainty of the estimated enthalpies of the bubbles.

One way to explain the apparent correlation is if the outer bubbles were not produced by a single outburst but rather constituted of merged bubbles from various generations

(Panagoulia et al., 2014). This would effectively make more distant bubbles bigger and explain why higher values of enthalpies are obtained. It would also mean that newer bubbles were faster than the old ones. Thus a mechanism which would substantially slow the bubbles down at large distances would be required.

Another possible explanation lies in the assumption that all the bubbles are undergoing continuous inflation rather than being produced by discrete outbursts. However among the sample studied in Diehl et al. (2008) large fraction of studied cavities consists of so called ‘ghost bubbles’. These bubbles do not emit any detectable radio emission and thus are assumed to be old. Nevertheless, the frequencies of the studied radio emission are limited and sometimes even apparently young cavities do not emit in radio. Thus this argument cannot distinguish whether inflation is continuous or discrete on its own. Moreover, in case of Hydra A, based on radio observations, it was uncovered that the cavities from different generations are connected via narrow channels out to a few kiloparsecs (Diehl et al., 2008). Such a channel was reported for NGC 5813 as well (Randall et al., 2015). These features could also help to explain how is the energy transported from the bubbles to the surrounding medium.

Furthermore, from hydrodynamical simulations Brügggen et al. (2009) concluded that the correlation is a result of the angle under which the bubbles are observed. For jet axis inclined by 45° with respect to the line of sight, the inferred energy grew hardly at all whereas for the case where the jet axis lies in the line of sight it grew by a factor of 2. However, this explanation requires to presume the intrinsic shapes of the cavities to be known.

To summarize, the computation of enthalpy of the bubbles as function of pV is highly dependent on the validity of the assumption of pressure equilibrium with its surrounding. Moreover, it strongly depends on the determination of the bubble sizes which is governed by large uncertainties. The reason for apparent correlation between the enthalpy of the bubbles with its distance is unclear although number of possible explanations exist. As a result, the computed values ought to be considered only an estimate.

1.4.6 Power of the jets

In order to determine the power of the jets, it is assumed that most of the energy deposited by it is used for the inflation of the cavities. Since observed shocks are mostly weak or none existent (McNamara and Nulsen, 2007) and radio losses are generally negligible (Birzan et al., 2004) this assumption appears to be sufficiently accurate. Thus in order to determine the power of the jets only the enthalpy of the bubbles together with their age estimate is needed.

Apart from approximations mentioned so far, the losses of energy via sound waves, thermal conduction and cosmic ray leakage are neglected (McNamara and Nulsen, 2012). In some cases, pieces of the bubbles may broke away as they rise and the relativistic particles from inside may leak, as is observed in Perseus Cluster (Birzan et al., 2004). This can lead to underestimation of the power of the jets.

Furthermore, the power of the jet is computed under the assumption that it is constant on time scales of \sim Gyr it takes for the bubbles to rise. However, it is not clear whether this

1.4. Cavities – their formation and properties

assumption is always valid, since cases where the powers found from different generation of cavities differ exist, suggesting variability. However, these differences are mostly within the uncertainties of the computation.

To summarize, the inferred powers of the jets are most strongly dependent on the estimated enthalpies of the bubbles. And the greatest source of uncertainty of these are the estimated sizes of the cavities.

Chapter 2

X-ray data processing

2.1 Chandra and ACIS

The Chandra X-ray Observatory (CXO) is NASA's successor of the Einstein Observatory. It was launched in July 1999. Even though the first launch attempt was unsuccessful due to a faulty sensor and the second was cancelled because of a near thunderstorm, the third attempt managed to get the observatory in orbit if not without complications. (For details, see Schlegel (2002).)

Being on a highly elliptical orbit with perigee at 19 400 km and apogee as far as 130 000 km¹, the observatory has an orbital period allowing more than 48 hours of uninterrupted observation before reentering the Earth's radiation belts. One of the most remarkable features of Chandra observatory is its unmatched spatial resolution of 0.492 arcsec. Another important characteristic is a high-resolution spectroscopy in 0.08 – 10 keV (15 – 0.12 nm) range. (Weisskopf et al., 2002)

The spacecraft carries a high resolution mirror, two imaging detectors and two sets of transmission gratings. In this work, for spectral analysis only one of the Advanced CCD (Charge coupled device) Imaging Spectrometer (ACIS) S3 was used. This chip is on axis with the best energy resolution of the ACIS system. Its field of view is 8.4 x 8.4 arc minutes. (Garmire et al., 2003)

The S3 chip is back illuminated (BI) metal-oxide-semiconductor (MOS) CCD. Thus, the quantum efficiency (QE) at low energies (which are of interest in this work) is much higher than for a front illuminated (FI) CCD. However, for this type of detector, the noise tends to be higher. Furthermore, since the surface is rather thin, it is more vulnerable to defects introducing charge-transfer inefficiencies (Arnaud et al., 2011). Nevertheless, the QE variation with position on BI chips is much smaller than for FI chips. This is mainly a result of relative insensitivity of the BI chips to cosmic rays and consequent afterglows.

¹<http://www.heavens-above.com/orbit.aspx?satid=25867>

Problematic and unforeseen issue is molecular contamination causing continuous decline of effective area at energies below 2 keV. It is caused by freezing of the out-gassed material on the cold ACIS optical blocking filters.² Even though the build up is being monitored, it is not easy to calibrate and thus it is unclear, how much are obtained data contaminated by this effect. Nevertheless, the data used here are archival and thus were obtained when the contamination was not so severe as it is now.

2.2 Backgrounds and foregrounds

Apart from the X-ray radiation of the studied source, various backgrounds and foregrounds obscure our view. This section describes cosmic backgrounds as well as instrumental backgrounds and how they contribute to the observed emission. (For more thorough overview, see Arnaud et al. (2011).)

2.2.1 Instrumental backgrounds

The signal seen when the instrument is not exposed to X-rays is called the particle background. It is caused by the interaction of charged particles with the detector or the material surrounding it. Chandra measures this background for ACIS when the detector is in stowed position since it cannot close its filter wheel.

The particle background spectrum consists of continuum from particles interacting with the detector as well as lines caused by X-ray fluorescence and interaction with the surrounding material. The shape of the particle background varies with time. Nevertheless, standard background files are available. These are easily scaled to each observation based on flux in 9 – 12 keV band in which the instrumental response to cosmic X-rays becomes negligible while the response to particles does not.

Another source of instrumental background is the soft-proton contamination. The Sun produces soft protons (~ 150 keV) which are prone to be focused by the telescope in the same manner as the X-ray photons, making them indistinguishable from the actual signal. Furthermore, since their intensity depends on solar activity and is further modified by the Earth's magnetic field, they are highly time variable and unpredictable. Luckily, due to different orbital paths, their contamination is not nearly as severe for Chandra as is for XMM-Newton. Nevertheless, parts of the observations contaminated by them cannot be used. Their presence can be identified based on the measured flux since the flux of the studied source is considered to be constant over the exposure time.

2.2.2 Cosmic backgrounds

The main source of extragalactic background in the 0.1 – 10 keV band are unresolved AGN. Their spectrum can be characterized by a power law. The fainter AGN tend to have flatter spectra than the bright ones

Furthermore, the galactic foreground contributes to the detected signal. The Local Hot Bubble is an irregular region surrounding the Sun with a radius of 100 – 200 pc. It consists

²<http://cxc.harvard.edu/>

of gas with a temperature of 10^6 K and its emission can be seen in every observation. On the other hand, the Galactic Halo with temperature $1 - 3 \cdot 10^6$ K typically emits from beyond the bulk of neutral disk gas and thus is absorbed to various degree depending on the position of the studied source.

Additionally, when ions from solar wind interact with the neutral ISM or the uppermost layers of Earth atmosphere, they exchange an electron via process called solar wind charge exchange (SWCX). This results in X-ray emission variable on timescales from hours to weeks. The charge-exchange spectrum is composed entirely of lines. However, since the ionization structure of the solar wind changes so does the ratios between individual lines. Thus, the identification and description of the exact spectral shape of this contamination is not easy and there is no way to determine the total extent of the SWCX contribution.

2.3 Observations and data reduction

2.3.1 Imaging techniques

Since imaging techniques are key to cavity detection, they are in depth described in the next chapter in sec. 3.1. For details specific to individual galaxies, see the results in chap. 4.

For background subtraction, blank sky background files were used.³ All exposure corrections were done with mono-energetic exposure maps created with the CIAO tool *mkexpmap*. The images of the individual observations were reprojected on one of the ObsIDs with python module *reproject* and then combined. The image operations such as subtraction and division were carried out by the CIAO *dmimgcalc* tool.

2.3.2 Extraction of the spectra

For spectral fitting of NGC 4649 six archival *Chandra* observations were used, listed in table 2.1. Together they give a total exposure time of ~ 280 ks. All of them have aimpoint on chip S3. For data reduction X-ray processing package CIAO version 4.9 with calibration database (Caldb) version 4.7.7 were used following the standard data reduction threads available at <http://cxc.harvard.edu/ciao4.9/>.

After reprocessing the datasets using *chandra_repro* script with flagging for VFAINT events, light curves in 0.5 – 7.0 keV band were extracted with *dmextract* and examined. Only observation 785 showed signs of significant flaring. The detection of point sources was aided by the *wavdetect* tool, however the list of detected sources was further visually inspected and modified. For spectral extraction, CIAO tools *dmellipse* and *dmextract* were used to create concentric, contiguous annuli depicted in fig. 2.1. Each annulus contains at least 6 000 photons out to 1 kpc radius and 10 000 photons to 6.5 kpc. Extraction of spectra further out was avoided in order to keep the extracted region on every observation at least 16 arcsecs from the chip edge where the response is uncertain due to dithering of the telescope. The position of the center of the extracted regions was determined for each

³For unsharp masking as well as GGM filtering, the background was sometimes neglected since these techniques highlight the relative differences and gradients. Because the background is assumed to be uniform and small across the exposure corrected images it does not have a notable influence on them.

ObsID	Total exp. time (ks)	Cleaned exp. time (ks)	Start date (UT)
785	38.12	21.78	2000-04-20 03:33:01
8182	52.37	49.46	2007-01-30 12:29:37
8507	17.52	17.52	2007-02-01 02:55:52
12975	84.93	84.93	2011-08-08 07:30:06
12976	101.04	101.04	2011-02-24 17:30:07
14328	13.97	13.97	2011-08-12 01:35:37

Table 2.1: Chandra observations of NGC 4649 used for spectral fitting and image processing.

observation based on visual inspection in order to account for astrometric offsets⁴ between individual observations. The magnitude of the offsets was found to be always less than 1 arcsec.

The spectra were extracted with the *specextract* script and grouped to contain at least 1 count per bin to validate the use of C statistics. As background, the standard blanksky background files were used, scaled by the 9.0 – 12.0 keV particle background and filtered for VFAINT events.

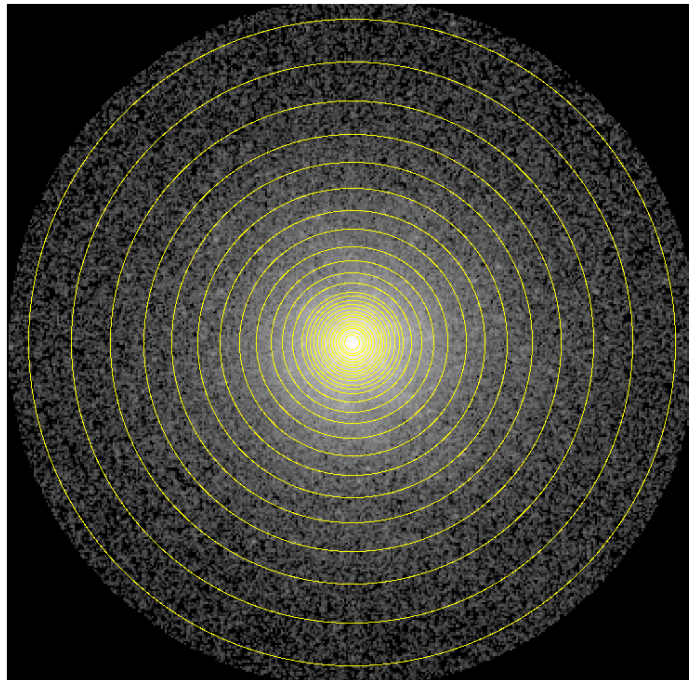


Figure 2.1: The annuli used to extract spectra. Each annulus contains at least 6 000 photons out to 1 kpc and 10 000 photons out to 6.5 kpc.

⁴Correction of the astrometric offsets by reprojection was considered and tried but since it relies on exact positions of the detected sources which were partially identified by eye, it introduced greater offsets than it corrected.

2.3.3 Spectral data analysis

Spectral fitting was carried out in the 0.6 – 2.5 keV band independently in two software packages in order to compare them and get a rough estimate of the systematic uncertainty stemming from the use of different plasma codes.

In XSPEC version 12.9 (Arnaud, 1996), the ISM emission was modeled as emission spectrum from collisionally-ionized diffuse gas with *apec* model. The abundances of all elements were tied to the iron abundance. Furthermore, the galactic absorption was modeled with multiplicative component *phabs*. The redshift was fixed at $3.706 \cdot 10^{-3}$. The cross-section was set to *bcmc* from Balucinska-Church and McCammon (1992) with a new He cross-section based on Yan et al. (1998). The hydrogen column was fixed to value $2.1 \cdot 10^{20} \text{ cm}^{-2}$ adapted from the Leiden/Argentine/Bonn survey (Kalberla et al., 2005). Cosmology with $H_0 = 70 \text{ km/s/Mpc}$, $q_0 = 0$ and $\Lambda_0 = 0.73$ was assumed.

The second used software package was SPEX version 3.03 Kaastra et al. (1996). Here, to model the ISM emission, additive *cie* component was used. The abundances of all elements were similarly coupled to iron. Perhaps counterintuitively, multiplicative component *hot* with temperature fixed at 0.5 eV was used to represent the influence of cold plasma causing the galactic absorption.

In order to compensate for projection effects, deprojection was conducted under the assumption of spherical symmetry. In XSPEC multiplicative component *projct* was used. Since SPEX does not support deprojection at present, the spectra were first deprojected with DSDEPROJ Russell et al. (2008) before being fitted in SPEX. While χ^2 statistics was used for this fit, in all other fits, C statistics of Cash (1979) was employed. As a minimization method served Monte Carlo. The distance of 16.5 Mpc for NGC 4649 was adapted from Blakeslee et al. (2009), giving scale of 1 arcsec = 79 pc.

Results reported in the following chapters are with 1σ uncertainties unless stated otherwise and error bars along the x-axes represent the width of the annuli. The results of spectra analysis were processed with Python and its specialized libraries Scipy, Numpy and Matplotlib.

Chapter 3

Cavity detection

For estimation of the power of a jet, cavity size is required. However, determining its exact extent and location is non-trivial since there is no objective way for doing so. This chapter explores various imaging techniques which were used for cavity detection so far as well as the possibility of employing neural networks for the task.

3.1 Traditional imaging techniques

In order to determine the presence of the cavities and eventually their sizes and locations as accurately as possible, various imaging techniques for their detection have been carried out. In the following paragraphs, the individual techniques used are described along with all the applied parameter settings. For details specific to individual galaxies, see the results in chapter 4.

3.1.1 Unsharp masking

Unsharp masking has proven useful in the past to aid detection of structures (e.g. Fabian et al. (2003)). The technique requires to smooth the input image on two different scales, usually with Gaussian kernel. Afterwards, an unsharp masked image is created by a division of the large scale image by the small scale one. Since smaller structures tend to be smoothed out in the large scale image but not in the small scale one, the division of these two highlights these features. However, their sizes are influenced by the choice of the smoothing scales.

In this work, following the systematic search for cavities carried out by Shin et al. (2016), the CIAO *aconvolve* tool was used for creation of the smoothed images. As input image served a background subtracted exposure corrected image which had all detected

sources replaced by the *dmfilth* tool with POISSON method.¹ Background regions from which the values of counts that replaced the sources in the image were determined were annuli around the individual sources. For smoothing, Gaussian kernel was used with scales 10 pixels for the large and 2 pixels (i.e. 0.984") for the small scale image although different scales were tried out as well and found to be informative in some cases. (As the number of sigma to extend in each direction, value of 5 was used for both images.)

3.1.2 Beta modeling

The beta model is often used to describe the emission of the hot diffuse gas in elliptical galaxies as well as larger structures. The underlying assumption of the model is a spherical symmetry. The two dimensional beta model (Cavaliere and Fusco-Fermiano, 1976) used here is defined as

$$S(r) = S_0 \cdot \left[1 + \left(\frac{r}{r_0} \right)^2 \right]^{-3\beta+0.5} \quad (3.1)$$

where r_0 is the core radius.

In order to interpret the results of the fit, two images were made. The residual image was created by subtraction of the model from the input image and the normalized image by division of these two.

In order for the beta fit to be formally correct, the raw image ought to be fit along with the exposure map as a table and background modeled with a two dimensional constant. However, even when background subtracted exposure corrected images were fit and compared to the previous fits, no notable differences were found. Thus, exposure corrected images were used in some cases.

For fitting, the *Sherpa* package from CIAO was used. All parameters were kept free. Although the ranges of the position of the centroid were limited to smaller area around the core in order for a quicker convergence of the fit. For judging the goodness of the fit, modified C statistic was used and as a minimization method served Monte Carlo. For description of these, see the Sherpa documentation at <http://cxc.cfa.harvard.edu/sherpa/threads/>.

3.1.3 Gaussian Gradient Magnitude filter

The Gaussian Gradient Magnitude (GGM) filter² (Sanders et al., 2016b) is an edge detection method. It measures the gradient in the surface brightness distribution, assuming Gaussian derivatives with width σ . It is based on the assumption that cavities (and other astrophysical processes) are associated with density variations which result in surface brightness gradients. Those are then highlighted by the tool and depending on the choice of the magnitude of the parameter sigma, either small scale or large scale structures are

¹In order for the tool to function correctly, the input image was in some cases multiplied by an arbitrary constant. This ought to be of no importance for unsharp masking, since the smoothed images are divided by each other as well as for the beta modeling described below since the fit is unitless.

²Code available at <https://github.com/jeremysanders/ggm>

brought forth. For more in depth description as well as comparison with other image processing techniques, see Sanders et al. (2016b,a).

The application of the GGM filter is rather straightforward since it consists of only a short python script. The only free parameter is a number of sigma. With increasing value of sigma, larger features on bigger scales are highlighted. Since the cavities are of various sizes, different values of sigma were tried out. Especially small multiples of two were found to be most informative.

3.2 Novel methods based on Neural Networks

Various imaging techniques described above are used for the cavity identification. However, none of them seems to be applicable to all the known objects and when different methods are applied, different results can be obtained even though the same data are used. Thus, an objective and systematic way of defining cavity sizes is needed.

Inspired by Fort (2017), a convolutional neural network was created and trained in collaboration with A. Vojteková in order to detect cavities and determine their sizes. Rather than classical convolutional neural network, a series of inception-like modules was used since it offers a unique opportunity to study features on different scales at the same time. This is well suited for the cavity detection task considering that their sizes can greatly vary in dependence on their distance from the core. However, the number of real observations is not sufficiently large to train the network and the presence and extent of the cavities in them is questionable as well. Thus, a dataset of simulated observations was created. This section introduces some key terms, briefly describes the architecture of the network used as well as presents details about the creation of the training dataset.

3.2.1 Introduction

Neural networks potential for learning is limited by its size. Thus, it would seem that the most simple way of improving upon it would be to make the network bigger or in other words, deeper. However, this also makes the network more prone to overfitting, since it increases the number of free parameters and thus increases the capacity of the network to memorize the training dataset. Furthermore, the increased size of the network dramatically increases the use of computational resources. Any uniform increase of number of filters results in quadratic increase of computation.

Optimal solution to this problem offers the Inception module from GoogLeNet Szegedy et al. (2014). The Inception module increases the width of the network with lower risk of overfitting. Furthermore, it is also more computationally efficient equivalent to similarly performing networks with different architectures. The network used in this work resembles the Inception module while being significantly smaller. It is composed of series of convolutional blocks adapted from Fort (2017).

The convolutional blocks consist of several parallel blocks with various filter sizes. Each of these blocks can possess different number of kernels (types of filters). The filters in each individual layer share their weights across entire image since the features included in them are translationally and rotationally invariant. This means that it is useful for the filters

across the whole image to learn to detect the same features since they can be expected to appear at each location and thus the weights are tied together. This also significantly lowers the number of free parameters and therefore reduces the risk of overfitting. The architecture consists of several of these blocs stacked behind each other, each ended with batch normalization and 1 x 1 convolution.

Deeper in the network, the ratio of the bigger filters to the smaller ones ought to increase since the network is processing the information at higher level of abstraction where the features are spatially more sparse. However, bigger filters are computationally more expensive. Therefore, a balanced way of dimension reduction is required to make the network computationally plausible. For this purpose, each convolutional block is ended with 1 x 1 convolution which has a dual purpose. It is mainly used in order to reduce dimension in depth (the number of filters applied to each pixel), replacing computational bottlenecks that limit the size of the network. This increases the width of the network without significant performance penalty. Furthermore, they include rectified linear units (ReLU) as activation functions and therefore introduce non-linearity into the network. (Szegedy et al., 2014)

Non-linear activation function is required because other components of the network perform only linear operations on the filters. Thus, if no non-linear unit was included, the output of the network would always be a linear combination of its filters, significantly limiting its applicability to real life problems. Essentially, without non-linear activation function, the whole network would behave as one layer. The neurons would easily saturate and the network would quickly cease to learn. ReLUs have also proven to learn several times faster than equivalents with saturating neurons (Krizhevsky et al., 2012) and thus are a natural choice.

However, ReLUs were also found to 'die' when exposed to large gradients, since overly large gradients can cause the neurons to never activate again. Thus a slightly modified version of them was applied called Leaky ReLUs. Leaky ReLUs allow a small, non-zero gradient when the unit is not active and thus address the problem of dying by preventing the gradient from being zero. Nevertheless, while some authors claim this improved their networks performance, the results are not always consistent. (For more information, see <http://cs231n.github.io/neural-networks-1/#actfun>.)

Before the activation, the batch normalization is applied. The idea behind batch normalization is to normalize the inputs of each layer in such a way that they have a mean output activation of zero and standard deviation of one. This is analogous how the inputs of networks are standardized. While training deep neural networks, the distribution of each layer's inputs changes during the training, lowering the learning rates and making the network sensitive to parameter initialization. The batch normalization addresses these problems, preventing small changes to the parameters from amplifying into larger gradients. This prevents the training from getting stuck in saturated regions and also stabilizes the parameter growth. Furthermore, it provides a source of regularization to the network. This has been shown to be advantageous to network generalization and thus lowers the risk of overfitting. (Ioffe and Szegedy, 2015)

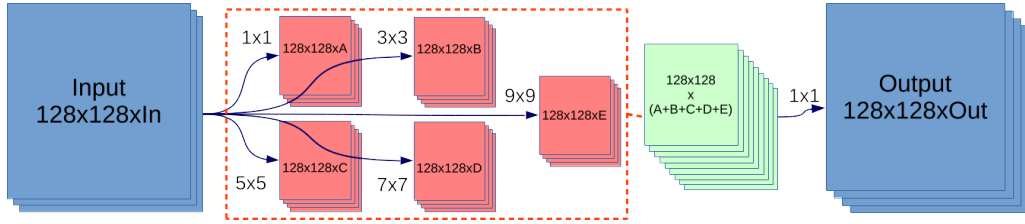


Figure 3.1: A diagram of one of the encoder blocks. The figure was adapted from Fort (2017).

3.2.2 The Network Architecture

The architecture is similar to that in Fort (2017). The network itself begins with an input layer. As input serve 128 x 128 images with normalized values. Afterwards follow four parallel blocks with five types of filters. There are A filters with sizes of 1×1 , B 3×3 , C 5×5 , D 7×7 and E 9×9 . The details of the block structure are shown in fig. 3.1. The numbers of filters in each block are presented in fig. 3.2. Each block is closed with 1×1 convolution. Finally, the network ends with a final block with 8×8 , 4×16 and 2×32 filters. Output is a pixel-wise cavity prediction. As a loss function serves a binary cross-entropy function. Furthermore, a slight change was made as opposed to Fort (2017). Instead of RELUs were used Leaky RELUs as was already discussed in section 3.2.1. For further information about the architecture, see Fort (2017).

All values of input images were increased by one and fed into a decadic logarithm to lower their ranges before entering the neural network.³ The network was trained on 180 000 images in 20 epochs in total where every epoch consisted of 9 000 images. As a result, the network has seen each training image four times in total, firstly unrotated, then rotated to the left by 90° , then unrotated again and lastly rotated by 90° to the right.

3.2.3 Creation of the dataset

The dataset of images of galaxies was generated based on physically realistic parameters from observational systematic studies. The images were generated under an assumption that exposure corrected, background subtracted images with replaced point sources will be used as input to the network. Only images from Chandra at aimpoint were considered therefore the size of the pixel was taken to correspond to 0.492 arcsec and Point Spread Function (PSF) was neglected due to its small size. A small constant background was added to the whole image in order to account for imperfectly subtracted background in the real images.

The size of the picture was taken to be 128×128 , corresponding to 1/16 of the ACIS chip. These dimensions were chosen mainly for computational plausibility of the network. The physical distance of the galaxies was drawn from the 15 – 100 Mpc range with a greater probability for galaxies in 25 – 65 Mpc range. The ellipticity was taken from 0.0 – 0.2

³The use of only a logarithm as a stretch function has later proved to be unsuitable since it fails to keep the ranges of values of all input images the same. This has resulted in a bias of the network towards certain ranges of values, as is discussed in sec. 5.4.



Figure 3.2: A diagram of the used architecture. An input image is fed into a sequence of 4 convolutional blocks, each containing presented number of filters. Afterwards follows the final layer (see text for details). The output is a pixel-wise cavity prediction where white indicates a high level of confidence that cavity is present. Batch norms and ReLUs are omitted for clarity. The figure was adapted from Fort (2017), modified.

range with greater probabilities of lower values. The angle of orientation was sampled randomly from $0 - 2\pi$ range. The position of the centre of the galaxy was constrained to area deviating from the middle of the image maximally by 4 pixels in both axis. Two types of galaxies were considered and in order to describe their emission, either single or double beta model was used.

For single beta model, the size of the core was drawn randomly from a range of $0.7 - 2.0$ kpc. Based on results reported in Dong et al. (2010), the beta index was randomly generated from $0.35 - 0.6$ range. In case of double beta model, the core radii were drawn from $0.1 - 0.4$ and $0.7 - 0.9$ kpc ranges. The ratio of the normalization of both components was constrained to $1.2 - 3.0$ range with a greater probability for values lower than 2.0. The beta index was taken from $0.2 - 0.3$ range.

Similarly as in Fort (2017), half of the dataset was created without cavities in order for the network to learn to distinguish whether cavities are present or not. For systems not further than 40 Mpc, the remaining half was then created with a pair of cavities in 75% of the cases and with two generations of the cavities in the remaining 25%. For galaxies further out, only one generation of cavities was considered. This was done in order to have the cavities fully constrained within the image.

For generation of cavity sizes, relation between the main axis and radius from Shin et al. (2016) was used with a slightly greater scatter than their cited uncertainties. This was done because it was assumed that the scatter was a physical one. Similarly, the size of the minor axis was based on the distribution of ellipticities determined from their data, modified to give greater preference to lower values.

The cavities were approximated as prolate ellipsoids lying in a plane perpendicular to the line of sight. This is not presumed to introduce a significant bias and thus hinder the detectability of cavities with different inclinations because their depth is so low compared to the emission of the host galaxy that the differences introduced by various inclinations

are negligible. The orientation of the cavities with respect to the direction of the jet was taken close to either radial or perpendicular elongation with the same probabilities. The depth of the bubbles was scaled relative to the emission at the position of their centers to be close to 10% with slightly varying ranges depending on the distance of the cavity from the AGN. The distance of the cavity from the center was limited to a range of 1 – 5 kpc for single cavity systems and 0.5 – 3 and 4 – 7.5 kpc for multicavity systems. The opposing cavities were allowed to deviate up to 2.5 degrees to either side of the jet. Furthermore, the cavities from the second generation could deviate from the jet direction in 0 – 20 degrees range as compared to the cavities from the first generation.

Three types of edges or rims composed of the gas which was originally at the place of cavities were considered. Either none, to account for cavities with weak shocks which already dispersed into the surrounding medium or are too weak to be observed (e.g. NGC 4649). Or cavities with edges only at the side close to the AGN like M84 or NGC 5846, where the outer parts were probably blown away by the momentum of the jet. And lastly, bubbles with full symmetrical rims similar to those of the innermost bubbles of NGC 5813. Each of these were generated with the same probability. The cavities of the same generation always shared the same type of the edge.

In total, 120 000 images with double beta profile and 60 000 images with single beta profile were created. For realization of the image generation, Python and its libraries Numpy, Random and Scikit were used.

3.3 Computation of uncertainties

The next chapter 4 lists the identified cavities along with their corresponding volumes, enthalpies, ages and finally, jet powers. This paragraph briefly describes the treatment of uncertainties stated there.

For judging the cavity position and dimensions, the previously discussed imaging techniques were used. The volumes were computed under the assumption that the true volume lies between the volume of prolate and oblate ellipsoid. Furthermore, a systematic uncertainty of 1 px stemming from the astrometric offsets between observations was also taken into account. For enthalpy calculation, the pressure was taken from the position in the middle of the bubble with uncertainties covering the one sigma errors of both SPEX and XSPEC values. As was discussed in sec. 1.4.3, the age was calculated under the assumption that the bubble moves at a speed of sound. Lastly, the powers corresponding to both bubbles were summed and their errors added in quadrature.

Chapter 4

Results

4.1 Detailed study of NGC 4649 (M60)

NGC 4649 is located in the Virgo cluster, 1 Mpc east of M87. It is currently undergoing ram pressure stripping due to its infall. Faint wings extending in the northern and southern directions are visible. Their direction is aligned with the jet axis. Otherwise, the galaxy appears very spherically symmetrical. To the northwest, a small satellite spiral galaxy NGC 4647 is present. (Wood et al., 2017)

The distance was taken to be 16.5 Mpc (Blakeslee et al., 2009), giving a scale of 79 pc per arcsec.

4.1.1 Radial profiles

Here are presented the results of deprojected spectral fitting with XSPEC as well as SPEX which are relevant for this thesis. In fig. 4.1 are the temperature and pressure profiles. The pressure was calculated as $p = nk_B T$. For density calculation a $n_e = 1.18 n_H$ ratio was assumed. The temperature profile peaks at the centre, is lowest at ~ 1 kpc where is the approximate location of the cavities and eventually rises again with increasing radius. The pressure profile peaks at the centre and follows a smooth distribution with only slight disturbance also present at ~ 1 kpc. It can be seen that the trend of obtained values of both fits is generally in agreement even when different plasma codes and deprojection techniques were applied. However, a systematic offset is present further discussed in sec. 5.2. The profiles deviate the most closer to the core. This is mainly a consequence of the deprojection, since all the uncertainties of all other values are propagating into the innermost bin.

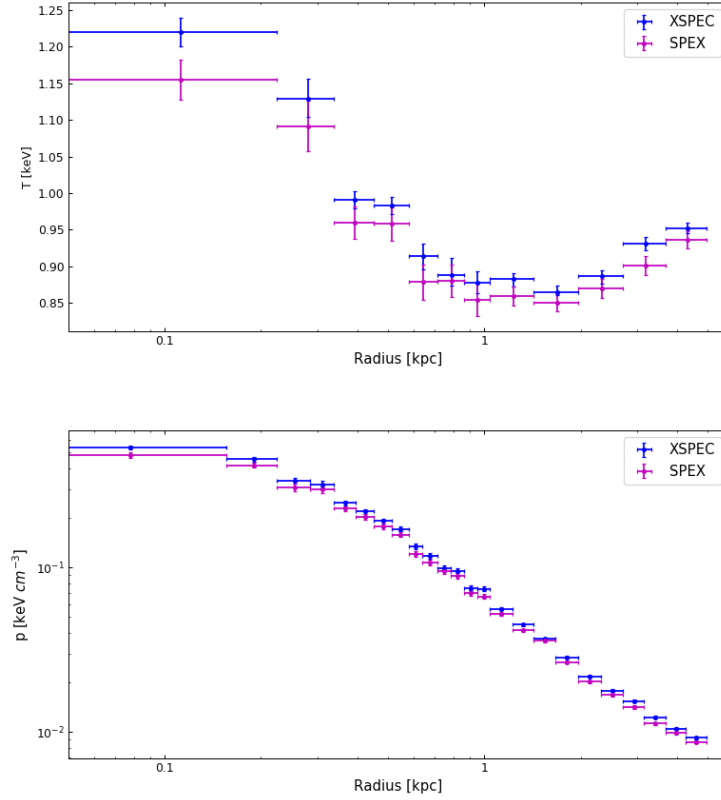


Figure 4.1: The deprojected temperature and pressure profiles obtained from fitting with XSPEC and SPEX. For details of the analysis, see section 2.3.3. The last point was excluded from the graph since it was influenced by emission from higher layers (annuli) which was not accounted for.

The Bondi accretion rate was calculated as $\dot{M}_{\text{Bondi}} = 4\pi\lambda c_s n r_A^2$ at accretion radius $r_A = 2GM_{\text{BH}}/c_s^2$ where λ is a numerical coefficient that depends on the adiabatic index of the accreting gas and is $\lambda = 0.25$ for $\gamma = 5/3$ (Bondi, 1952). The mass of the SMBH of $(4.5 \pm 1.0) \times 10^9 M_\odot$ was adapted from Shen and Gebhardt (2009). The maximal power released from the SMBH is then $P_{\text{Bondi}} = \eta \dot{M}_{\text{Bondi}} c^2$ for assumed efficiency of $\eta = 0.1$ (Allen et al., 2006).

r_A (kpc)	0.13 ± 0.03
kT (keV)	1.18 ± 0.06
n ($10^{-22} \text{kg m}^{-3}$)	8.1 ± 0.4
c_s (km s^{-1})	552 ± 13
\dot{M}_B ($M_\odot \text{yr}^{-1}$)	0.09 ± 0.02
P_B ($10^{43} \text{erg s}^{-1}$)	49 ± 11

Table 4.1: The Bondi parameters.

4.1.2 Cavity detection

The presence of the cavities in NGC 4649 has been mildly disputed in the past (e.g. Shin et al. (2016) concluded there are probably none based on X-ray data only while Shurkin et al. (2008); Dunn et al. (2010); Paggi et al. (2014) reported their presence based on X-ray and radio data but with different bubble sizes). Here, various techniques to confirm their presence and magnitude have been carried out.

The same observations as those used for spectral fitting were used for image processing (see tab. 2.1). For all exposure corrections, mono-energetic 0.9 keV exposure maps were used. The images of the individual observations were reprojected on the ObsID 785. The 0.6 – 2.5 keV energy range was used.

Unsharp masking

While the input image shows signs of cavity presence to the north and south, their depth is very low. The unsharp masked image shows them more clearly. They appear as rather small, circular depressions in the surface brightness. In fig. 4.2, raw image is presented as well as both the large (10) scale and the small (2) scale smooth images, along with the unsharp masked one.

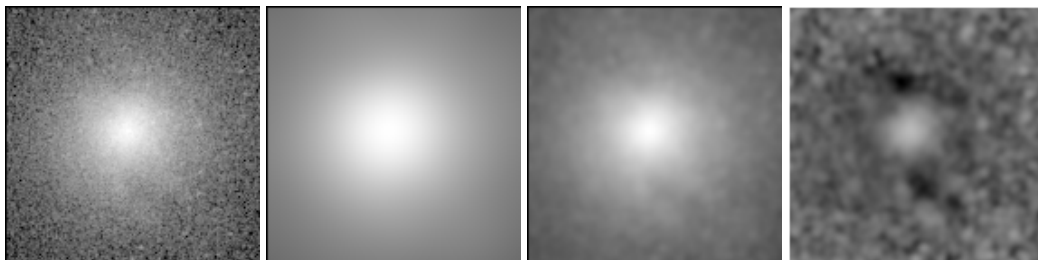


Figure 4.2: From left to right are presented the input image, smooth image with scale 10 sigma, smooth image with scale 2 sigma and the unsharp masked one. The sizes of all images of NGC 4649 are 70 x 70 arcsecs, corresponding to 5.5 x 5.5 kpc, unless indicated otherwise.

Beta model and other models

Since this galaxy seems very spherically symmetrical, it can be well described by the beta model and therefore an excellent fit with reduced value of modified C statistics 1.16 was obtained. In the fig. 4.3 below are presented next to each other the beta model, the residual image and the normalized image.

Because the residuals close to the core are significantly bigger than those at larger radii a fit with slightly different profile was carried out in order to determine whether they are real structures or signs of over and under subtraction. For this fitting, the same annuli that were used for the spectral fitting were used. Each of them was fit in *Sherpa* with constant background and a King function adopted from (Eckert et al. (2016), Appendix B). The value of most of the parameters was fixed at values determined from a global fit of the whole galaxy. The r_c was frozen in the middle of each annuli. Only the normalization

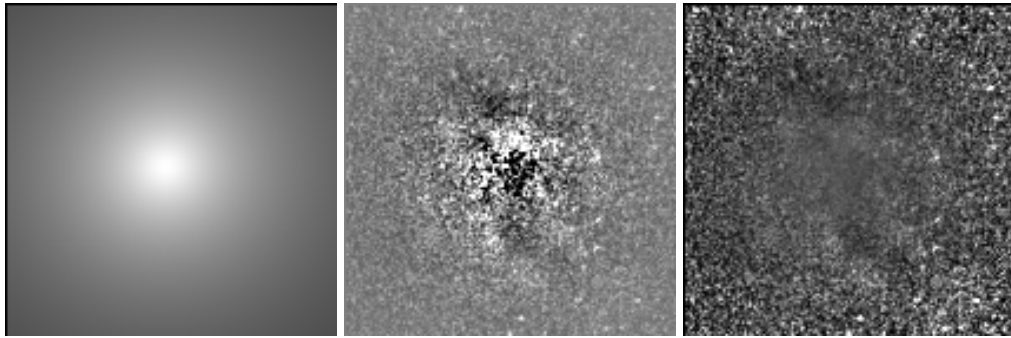


Figure 4.3: From left to right: The beta model, residual image (created by a subtraction of the model) and the normalised image (created by a division by the model).

and parameter β were kept free. However, the resulting residual image obtained by this technique is virtually indistinguishable from the one obtained by simple beta fit. But while in the outer parts an excellent fit with reduced values of statistic close to 1.0 were obtained closer to the core where the cavities are present, the quality of the fit worsened up to ~ 1.6 .

Furthermore, the bias introduced by the assumption of the spherical symmetry was investigated to some degree by allowing the ellipticity and theta parameters to vary. Since in reality the elliptical galaxies are believed to be closer to triaxial ellipsoids rather than perfect spheres if we observe such a body under any angle unaligned with any of its axis, the ellipticity would be changing as a function of radius (Sarajedini, 2017). The results seem to suggest that this bias is unimportant for our purposes because even though various values of best fit ellipticities were obtained for different annuli and at some, slightly statistically better fit was obtained, the residual image remained practically unchanged.

Therefore, it is not entirely clear if the residuals are associated with real features. Problematic is that they can be created in various ways. For example the gas sloshing can produce asymmetry or faint cold fronts which are not directly observable and can also create residuals similar to cavities.¹ However, these effects are not believed to be important here. It is also noteworthy that the bright residuals are perpendicular to the direction of the jets which is a property that does not seem to be unique to this system (e.g. see Abell 262 in Shin et al. (2016)) while it does not seem to be generally applicable either.

Moreover, from fitting with Sersic profile, it was discovered that the core² cannot be fitted with it adequately. However, for the outer parts, equivalently good fit was obtained as is the fit with beta profile. Again, the residuals are not presented since they are virtually indistinguishable from those of a beta fit. Thus, it would seem that the bright residuals near the core are the result of the fact that the emission of the core is probably governed by different physics (Kormendy et al., 2009) and thus cannot be described by the model well.

As a result, it would seem plausible that the residuals extending over the radio core ought not to be taken into account while judging the position and extent of the cavities.

¹As was pointed out by P. E. J. Nulsen, private communication.

²As the core is here considered the radio core visible in fig. 4.4

GGM filter

The images processed with the GGM filter with sigma sizes of 2 and 4 are in fig. 4.4. Since the ability of the GGM filter to detect a gradient in surface brightness depends among other things on the magnitude of the jump Sanders et al. (2016a) and the surface brightness depression at the location of the cavities is rather low, their presence is only hinted in the GGM filtered image. However, even though the inner parts of the cavities are not visible, hints of the outer parts are present. This is the exact opposite of the raw image where only the inner parts of the cavities are clearly distinguishable. It is also worth noting that the projection effects are not accounted for in this image (as well as all other images), which can also influence the ability to detect cavities. However, this effect ought not to be of great importance here since only the relative brightness depressions relative to the immediate surroundings which are subject of the same projection effects are judged here. Nevertheless, the projection can be expected to be the strongest near the core.

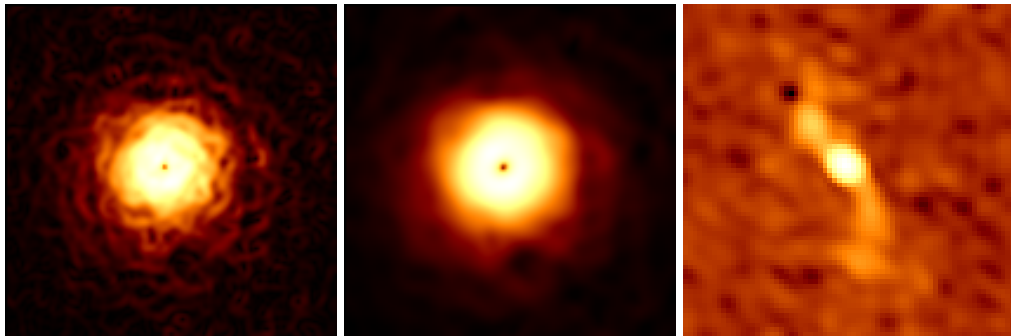


Figure 4.4: From left to right are presented the GGM filtered images with sigma sizes of 2 and 4 and the radio image at 1.4 GHz kindly provided by R. Dunn.

Interpretation of the results, comparison with radio emission

Based on all the techniques mentioned above, cavities are indeed believed to be present. Their existence was previously also reported in Shurkin et al. (2008); Dunn et al. (2010); Paggi et al. (2014). Furthermore, interesting notion indirectly supporting this as well is a suggestion by Wood et al. (2017). They studied the outer parts of NGC 4649 and noted that it has filamentary wings aligned with the direction of jets. Thus, it may be possible that the gas in them was uplifted there by previous AGN outbursts.

Nevertheless, the exact extent of the cavities is not entirely clear since the peak of the radio emission in the VLT 1.4 GHz image is at a different location, much closer to the core (see fig. 4.4). Therefore, it might be possible that two generations of cavities close by are present. Since the inner ones would be younger, they would be much brighter in radio. They also seem only very mildly visible in the X-ray flat-fielded image. The outer ones are much clearly seen in the X-ray and if they are on the verge of becoming ghost cavities, that might explain why are they not clearly visible in radio. However, their location relative to radio emission seems rather strange nevertheless. Questionable also seems that the relative intensity of the radio emission for inner cavities. The north cavity's

intensity seems twice as large as the south one. Moreover, their shapes quite differ. This might be the result of projection effects combined with relativistic effects, which are both connected to the unknown inclination. However, it does not seem that these effects are the only source of differences between both cavities. Worth noting is also a correlation between projected minor and major axis of cavities reported for numerous objects in Shin et al. (2016), suggesting that the projection effects are not greatly misrepresenting the true cavity sizes in general.

In previous works using shallower (Shurkin et al., 2008; Dunn et al., 2010) as well as the same (Paggi et al., 2014) observations, the scenario with one generation of cavities was assumed. However, the sizes and location of the cavities found in these works differ. In this work, it was also found to be more likely that there is indeed one generation of cavities present. Not only is the evidence for second generation of cavities inconclusive but also if that were the case, based on scaling relation between cavity size and its distance discussed in section 1.4.1, the sizes of the outer bubbles would be expected to be much larger. Furthermore, the radio emission of the southern lobe does not seem to be separated at all and this is in agreement with the residuals of the beta model.

Cavity detection

Based on the techniques mentioned above, the cavity sizes and locations were estimated and are presented in fig. 4.6. For comparison, alongside are also shown the cavity sizes determined by Paggi et al. (2014) using the same data and relying on beta modeling and by Dunn et al. (2010) using shallower X-ray as well as radio data. However, they primarily relied on beta model as well. Furthermore, in fig. 4.5 is presented the cavity prediction of the neural network. It can be seen that the network has not only detected the bubbles but with less confidence also a region at the right side of the image where comparable surface brightness depression is present. The outputs of the network are further discussed in sec. 5.4. All the determined bubble sizes along with the corresponding enthalpies, ages and powers are presented in tab. 4.2.

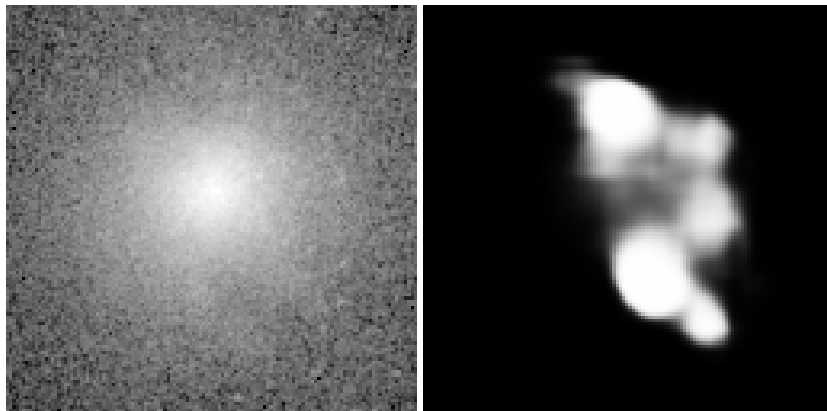


Figure 4.5: The input image and the resulting pixel-wise cavity prediction of the neural network. Higher values denoted by white indicate high level of confidence that cavities are present. The dimensions of the images are 5 x 5 kpc.

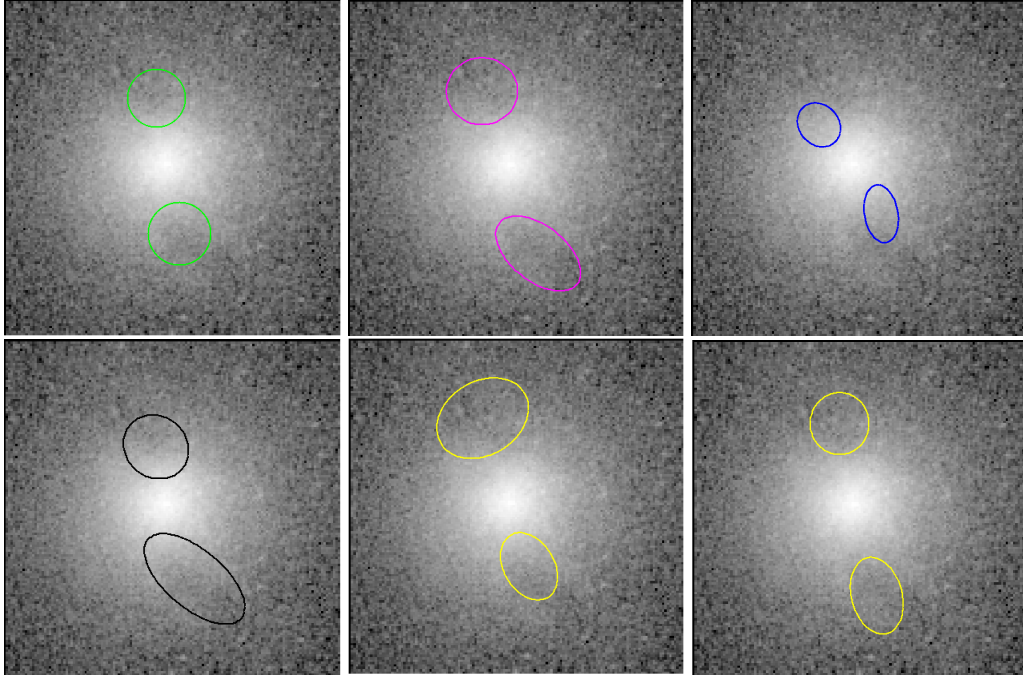


Figure 4.6: The cavities determined from different methods. From left to right: The cavities based on the unsharped masked image, beta modeling, radio observation, the prediction of the neural network and as they were estimated by Paggi et al. (2014) and by Dunn et al. (2010).

Method	R (kpc)	a (kpc)	b (kpc)	V (10^{57} m^3)	$E = 4pV$ (10^{54} erg)	t_{age} (Myr)	P_{jet} ($10^{41} \text{ erg s}^{-1}$)
UM	1.05	0.52	0.48	$15.6^{+2.8}_{-2.4}$	$13.1^{2.6}_{-2.3}$	1.86 ± 0.04	4.1 ± 0.3
	1.21	0.57	0.52	$20.2^{+3.3}_{-2.9}$	$13.0^{2.2}_{-2.0}$	2.15 ± 0.05	
Beta	1.26	0.67	0.55	$27.5^{+4.1}_{-3.6}$	$14.1^{2.2}_{-2.0}$	2.22 ± 0.05	4.2 ± 1.7
	1.58	1.06	0.46	$45.5^{+6.1}_{-5.5}$	$19.5^{2.7}_{-2.5}$	2.80 ± 0.07	
Radio	0.82	0.41	0.33	$6.1^{+1.5}_{-1.3}$	$6.7^{+1.8}_{-1.5}$	1.45 ± 0.03	2.5 ± 0.8
	0.98	0.52	0.28	$7.1^{+1.8}_{-1.5}$	$5.9^{+1.6}_{-1.3}$	1.73 ± 0.04	
NN	0.92	0.63	0.50	$21.8^{+3.5}_{-3.0}$	$18.8^{+3.3}_{-2.9}$	1.63 ± 0.04	10.1 ± 5.5
	1.36	1.58	0.48	96^{+11}_{-10}	$49.2^{+6.3}_{-6.0}$	2.41 ± 0.06	

Table 4.2: Parameters of the cavities determined from unsharp masking (UM), beta modeling, radio data and by neural network (NN) along with corresponding timescales and powers of the jets. First is listed the northern cavity.

4.2 Application to other galaxies

All the radio data at 1.4 GHz were kindly provided by R. Dunn except for M84 where the contours were contributed by A. Finoguenov. The pressure and temperature values used for sound speed and jet powers calculations were supplied by K. Lakhchaura.

4.2.1 NGC 4472 (M49)

NGC 4472 is the brightest group galaxy located at the outskirts of the Virgo cluster, currently falling in it (Joseph et al., 2017). It is the most optically luminous galaxy of the local Universe (Gendron-Marsolais et al., 2017). Its distance was taken to be 16.7 Mpc (Blakeslee et al., 2009), giving a scale of 81 pc per arcsec.

For input image creation, archival observations 321, 11274, 12888, 12889, 16260, 16261 and 16262 were processed, adding up to a ~ 437 ks deep image. While even more observations exist, they were not used due to their short exposure times, since their influence on the combined image would be negligible. For all exposure corrections, monoenergetic 0.925 keV exposure maps were used. Individual observations were reprojected on ObsID 321. The 0.5 – 2.0 keV energy range was used.

Cavity detection

The X-ray emission of NGC 4472 clearly shows two cavities. They appear as incomplete and given their short distance from the core rather large ellipses, easily identifiable due to enhanced rims encircling them. Their orientation is quite different. While the left one is radially elongated the main axis of the right one spreads in a direction perpendicular to it. Surprisingly, even though the input image shows the cavities quite clearly, they are rather hard to spot in the unsharp masked one (see fig. 4.7). As the most informative picture was chosen one with scales of 10 and 1 for the large and small smooth images, offering the least degree of modification of the original cavity shapes.

On the other hand, the beta modeling produced images showing the cavities quite clearly, as can be seen in fig. 4.8. Especially the normalized image shows them well. However, the region surrounding the core as well as the core itself show significant residuals. In order to reduce them, fit excluding the core emission was carried out. Nevertheless, this has resulted in a significant worsening of the quality of the fit to point where it became statistically unacceptable. Hence, only the fit including the core emission was used to judge the cavity extend.

Furthermore, the GGM filtered image with 8 sigma is presented. While it is highly

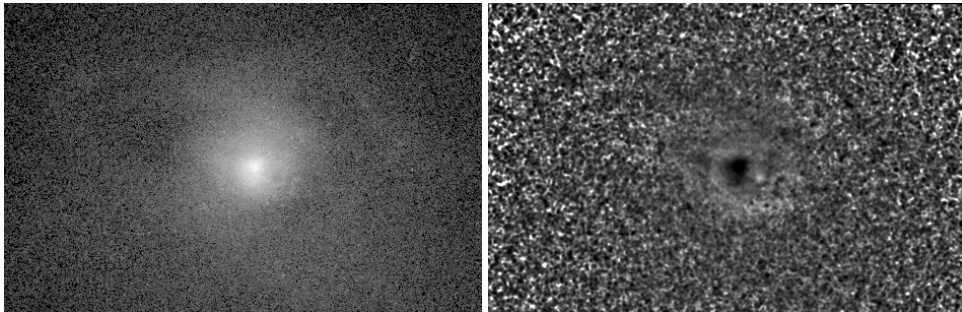


Figure 4.7: From left to right are presented the input image and the unsharp masked image from smooth images with scales 10 and 1. All images of NGC 4472 are 231 arcsecs wide and 149 arcsecs high, corresponding to 18.7 x 12.1 kpc.

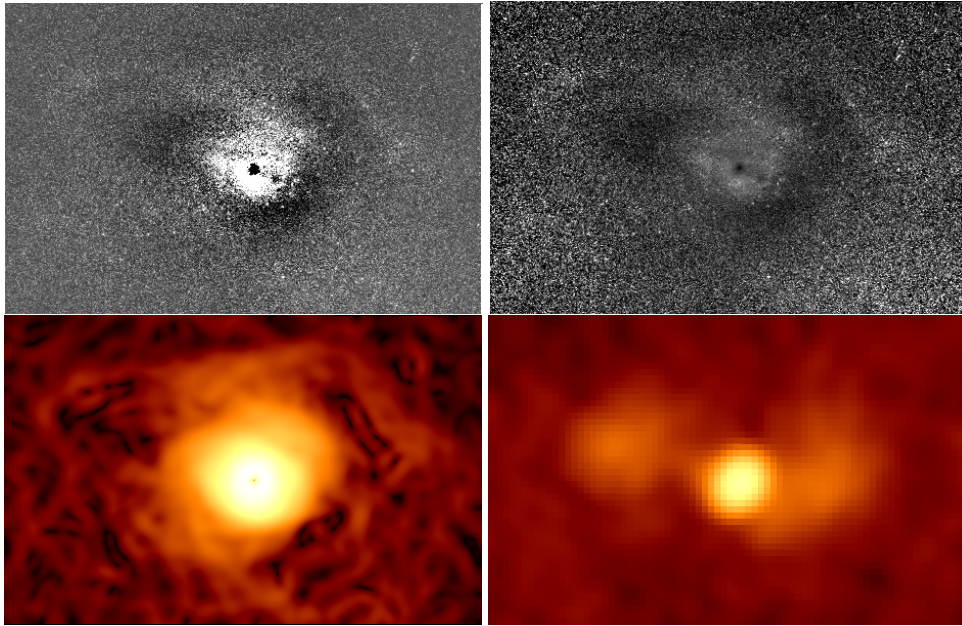


Figure 4.8: From left to right are presented the residual image and the normalized image based on the beta modeling, the GGM filtered image with 8 sigma and the radio emission.

indicative of the cavity presence, it does not show them particularly well. On the other hand, the radio emission shown alongside depicts pronounced radio lobes.

The output of the neural network is presented in fig. 4.9. The network successfully located both cavities but since it was presented with binned image, it underestimated the size of the west bubble as opposed to the other imaging techniques.

In fig. 4.10, the estimated cavity sizes based on techniques described above are shown, each overlaid over the input image. For comparison with cavities estimated by Gendron-Marsolais et al. (2017) see fig. 4.11. The cavity parameters are presented in tab. 4.3.

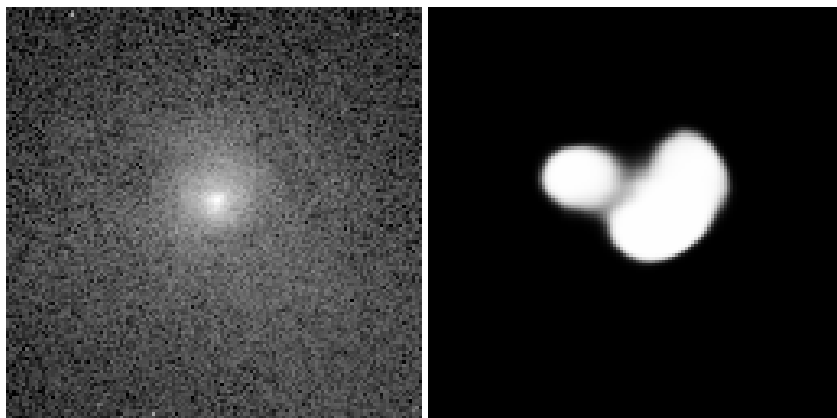


Figure 4.9: The input image and the resulting pixel-wise cavity prediction. Higher values denoted by white indicate high level of confidence that cavities are present. The sides of both images are equal to 20.4 kpc.

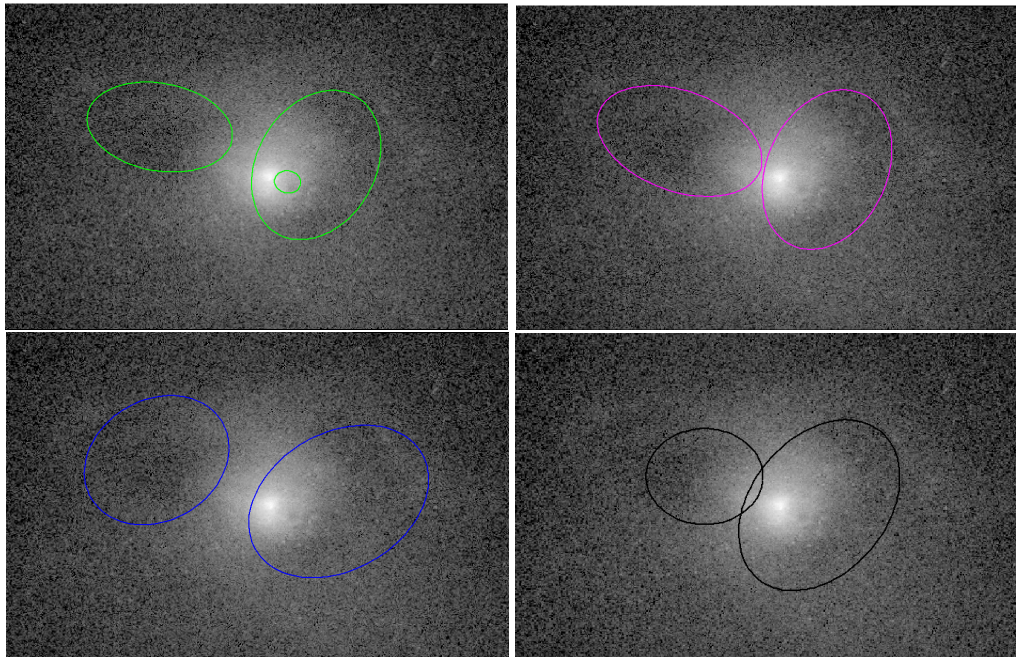


Figure 4.10: From left to right are presented the cavities as they were determined based on the unsharp masking, beta modeling, 1.4 GHz radio emission and by the neural network.

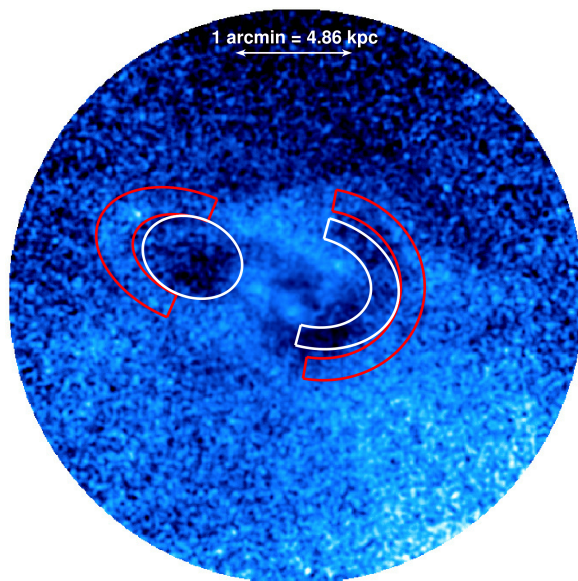


Figure 4.11: Beta residuals adapted from Gendron-Marsolais et al. (2017). Cavities are displayed in white. The bubble sizes were determined based on the same data as those used in this work. Compare with previous figure.

Method	R (kpc)	a (kpc)	b (kpc)	V (10^{59} m ³)	$E = 4pV$ (10^{56} erg)	t_{age} (Myr)	P_{jet} (10^{42} erg s ⁻¹)
UM	4.44	2.74	1.63	12.0 ± 0.5	1.27 ± 0.05	10.07 ± 0.02	5.3 ± 1.5
	1.83	2.95	2.21	20.6 ± 0.7	6.4 ± 0.2	4.14 ± 0.01	
Beta	3.95	3.20	1.87	18.7 ± 0.7	1.97 ± 0.07	8.95 ± 0.01	6.2 ± 1.9
	1.83	3.12	2.25	$23.2^{+0.8}_{-0.7}$	7.2 ± 0.2	4.13 ± 0.01	
Radio	4.51	2.82	2.25	19.9 ± 0.7	2.09 ± 0.07	10.23 ± 0.02	3.7 ± 0.8
	2.58	3.58	2.55	34.4 ± 1.0	5.7 ± 0.2	5.84 ± 0.01	
NN	2.97	2.18	1.78	9.4 ± 0.4	1.56 ± 0.07	6.72 ± 0.01	10.5 ± 2.1
	1.49	3.57	2.52	33.7 ± 1.0	10.5 ± 0.3	3.38 ± 0.01	

Table 4.3: Parameters of the cavities depicted in fig. 4.10. First is listed the western (left) cavity.

4.2.2 M84 (NGC 4374)

M84 is a radio-loud galaxy situated in the Virgo cluster (Walsh et al. (2010)). Its gas is highly perturbed and jet-like structure has been observed extending from the northern side of the core in 22 GHz observation (Nakahara et al. (2014)). A detailed study of this galaxy and energy content of its cavities is presented in Finoguenov et al. (2008). Its distance was taken to be 18.5 Mpc (Blakeslee et al., 2009), giving a scale of 90 pc per arcsec.

The input image is a courtesy of N. Werner. It was created from archival observations with ObsIDs 803, 5908 and 6131. The approximate exposure is ~ 115 ks.

Cavity detection

M84 posses a very complex morphology (see fig. 4.12), making it a rather unusual elliptical galaxy. While the presence of cavities is indisputable, approximating them as ellipsoids seems rather crude.

The cavities and their inner edges are clearly visible in the input image as well as the unsharped masked and smoothed one. However, that is not the case with the northern outer

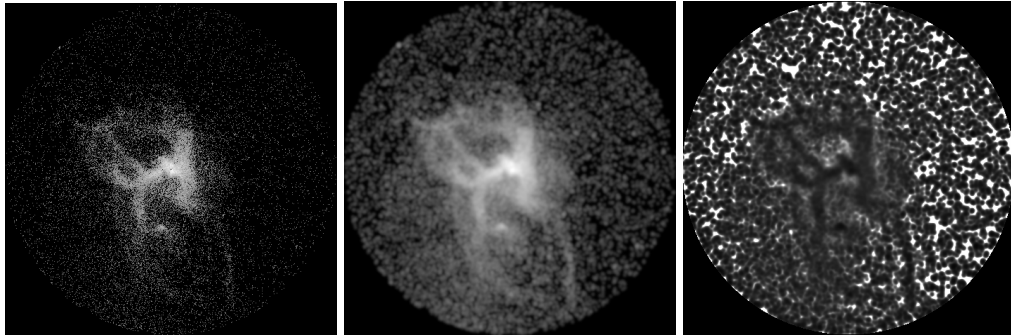


Figure 4.12: From left to right are presented the input image, the small (2) scale smooth image and the unsharp masked image from smooth images with scales 10 and 2. The sizes of all images of M84 are 232 x 232 arcsecs, corresponding to 20.9 x 20.9 kpc.

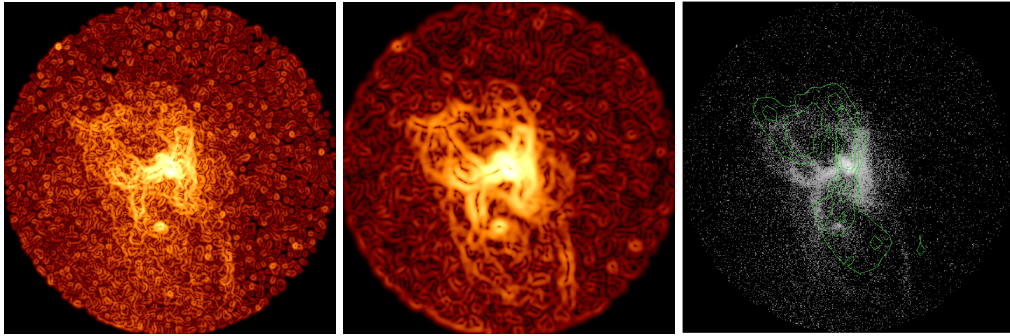


Figure 4.13: From left to right are presented the GGM filtered images with sigma 2 and 4 and the radio contours overlaid over the input image.

edge, where the radio emission has been observed to break through the bubble Finoguenov et al. (2008). Nevertheless, the outer edge of the southern bubble is nicely visible in the smooth and unsharped masked image.

While the bright rims make the cavity identification significantly easier in the unsharp masked image, the complex morphology causes a significant deviation from spherical symmetry as well. As a result, a statistically acceptable beta fit was not obtained.

On the other hand, the GGM filtered images nicely highlights the bright rims. In fig. 4.13, GGM images with sigma 2 and 4 are presented along with the radio contours overlaid over the input image. As opposed to the X-rays, the radio emission appears rather continuous and makes the distinction between the inner and outer pair of bubbles unclear.

In fig. 4.14, the prediction of the neural network is presented. It can be seen that even though the morphology of the galaxy is complex, the network successfully generalized to a non-elliptical shape of the bubbles.

Finally, the estimated cavity sizes are presented in fig. 4.15. For comparison, see also fig. 1 in Finoguenov et al. (2008). The parameters are listed in tab. 4.4 and the derived quantities in tab. 4.5.

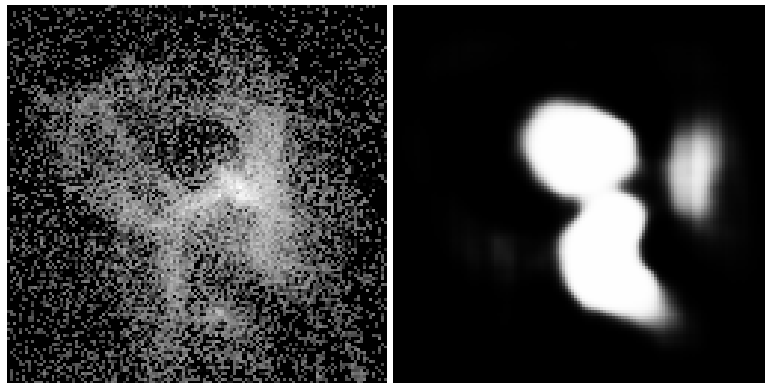


Figure 4.14: The input image and the resulting pixel-wise cavity prediction of the neural network. Higher values denoted by white indicate high level of confidence that cavities are present. The sides of both images correspond to 11.3 kpc.

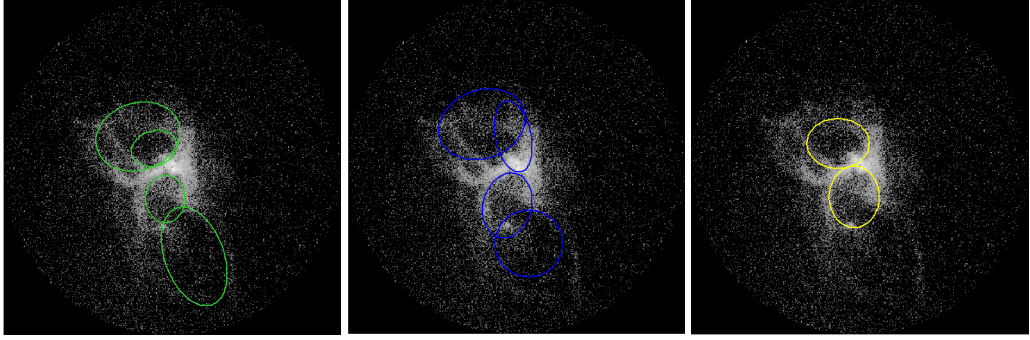


Figure 4.15: From left to right are presented the cavities identified from unsharp masking, radio emission and by the neural network.

Unsharp masking				Radio emission			
Cavity	R (kpc)	a (kpc)	b (kpc)	Cavity	R (kpc)	a (kpc)	b (kpc)
inner N	1.67	1.43	1.08	inner N	1.91	2.23	1.11
inner S	1.94	1.47	1.21	inner S	2.44	2.04	1.50
outer N	2.89	2.65	2.08	outer N	3.41	2.75	2.10
outer S	5.61	3.19	1.82	outer S	4.78	2.10	2.06

Neural network			
Cavity	R (kpc)	a (kpc)	b (kpc)
N	1.98	1.93	1.53
S	1.89	1.87	1.55

Table 4.4: Parameters of the cavities depicted in fig. 4.15.

Method	Cavity	V (10^{59} m^3)	$E = 4pV$ (10^{55} erg)	t_{age} (Myr)	P_{jet} ($10^{41} \text{ erg s}^{-1}$)
UM	inner N	2.4 ± 0.2	5.3 ± 0.4	4.17 ± 0.04	8.3 ± 1.4
	inner S	2.9 ± 0.2	6.5 ± 0.5	4.85 ± 0.05	
Radio	inner N	5.0 ± 0.3	$11.2^{+0.8}_{-0.7}$	4.76 ± 0.05	12.4 ± 4.6
	inner S	$6.6^{+0.4}_{-0.3}$	9.4 ± 0.6	6.08 ± 0.06	
NN	N	$6.3^{+0.4}_{-0.3}$	$13.9^{+0.9}_{-0.8}$	4.94 ± 0.05	18.0 ± 2.8
	S	6.2 ± 0.3	$13.6^{+0.9}_{-0.8}$	4.72 ± 0.05	

Table 4.5: Derived quantities of the cavities depicted in fig. 4.15.

4.2.3 NGC 5044

The NGC 5044 is an early type galaxy residing in the centre of the X-ray brightest group of galaxies with the same name. While the group has a very smooth and nearly spherically symmetric large-scale X-ray morphology, the galaxy itself is highly perturbed with many cavities, cool filaments, cold fronts, and multiphase gas. Furthermore, it is likely that the galaxy is undergoing a sloshing motion within the group centre in a plane perpendicular to the plane of the sky. (David et al. (2014) and references therein)

The distance of the galaxy was assumed to be 31.2 Mpc (Tonry et al., 2001), giving scale of 151 pc per arcsec.

For input image creation, all available archival observations were used – ObsIDs 798, 9399, 17195, 17196, 17653, 17654 and 1766. Together they contribute ~ 419 ks deep image. All of them were reprojected on ObsID 17195. For all exposure corrections, monoenergetic 0.975 keV exposure maps were used. The 0.5 – 2.0 keV energy band images were produced.

Cavity detection

The diffuse gas of NGC 5044 is greatly disturbed, showing many regions of surface brightness depressions as well as enhanced rims. Strangely, the bubbles do not lie in one axis as is commonly observed but appear to be aligned along two axes roughly perpendicular to each other, while the southern part of the vertical axis slightly bends to the west.

In fig. 4.16, the input image is presented along with the small (2) scale smoothed one which shows the bubbles perhaps more clearly than the original image and the unsharp masked one with scales of 10 and 2 sigma.

Perhaps surprisingly, given the degree of asymmetry of this galaxy, an acceptable beta fit was obtained. While the residuals (see fig. 4.17) engulfing the core seem questionable, the normalized image shows even this region clearly. A fit excluding the core region was performed as well but while the fitted parameters like r_0 and the amplitude changed quite

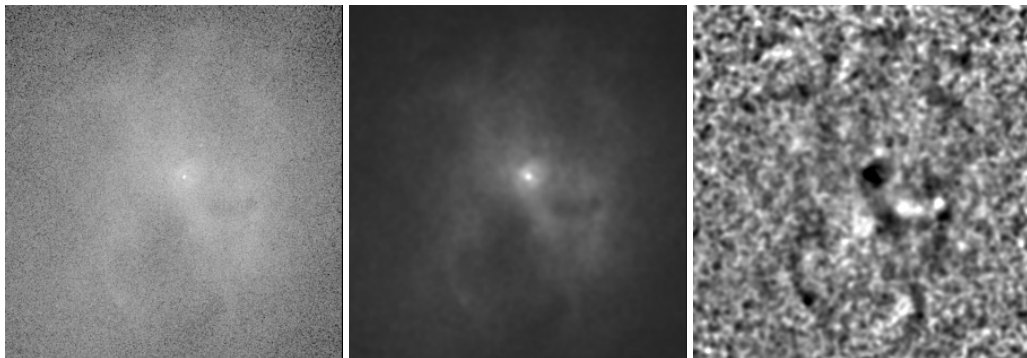


Figure 4.16: From left to right are presented the input image, the small (2) smooth scale image and the unsharp masked image from smooth images with scales 10 and 2 sigma. All images of NGC 5044 are 147 x 155 arcsecs big, corresponding to 22.1 x 23.2 kpc.

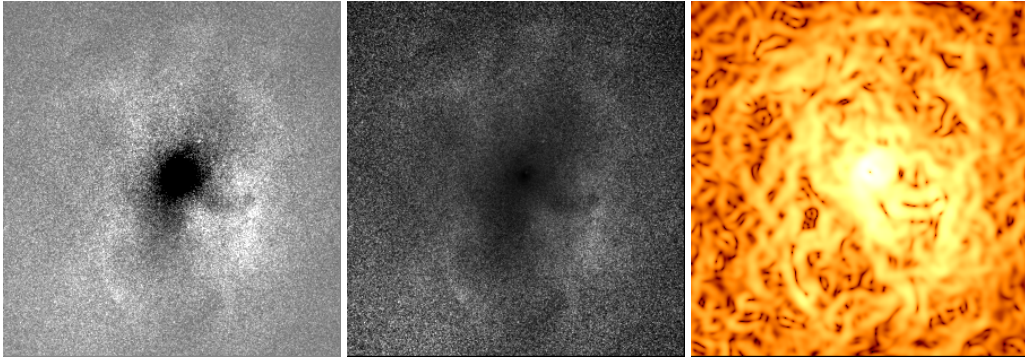


Figure 4.17: From left to right are presented the residual image and the normalized image based on the beta modeling, along with the GGM filtered image with sigma 4.

significantly, the resulting residuals were to the naked eye virtually indistinguishable from these presented here.

The GGM filtered image with sigma 4 is presented alongside. No detectable 1.4 GHz radio emission is present at the location of the cavities, only the core is radio bright.

In fig. 4.18 is presented the cavity prediction of the neural network. Only the most pronounced bubbles were detected. This is most likely a consequence of a bias concerning input image normalization present in the network and further discussed in sec. 5.4. Furthermore, the southern bubbles detected individually by unsharp masking and beta modeling were merged into one in the network prediction. This is probably a result of a necessity to bin the input image, degrading its quality.

In fig. 4.19, the estimated cavity sizes based on techniques described above are presented, each overlaid over the input image. Their distance from the core and semiaxis are listed in tab. 4.6. Furthermore, derived volumes, enthalpies and corresponding powers of the jets are listed in tab. 4.7.

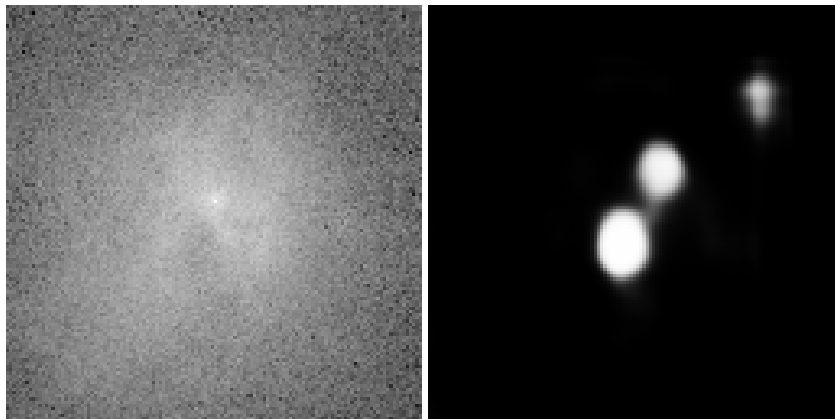


Figure 4.18: The input image and the resulting pixel-wise cavity prediction of the neural network. Higher values denoted by white indicate high level of confidence that cavities are present. The sides of both images are 38 kpc.

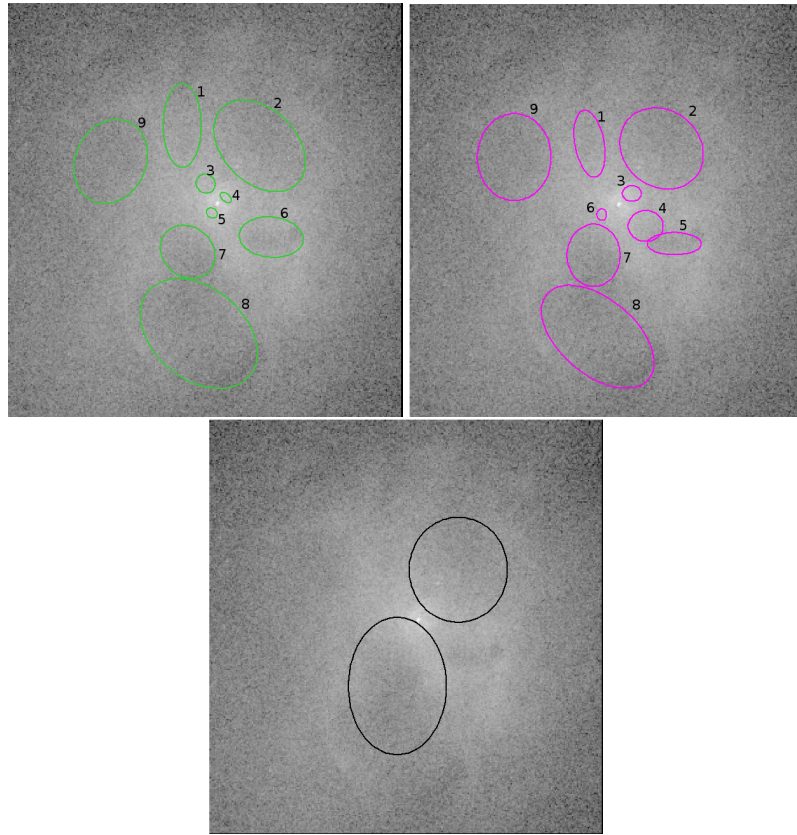


Figure 4.19: From left to right are presented the cavities as they were determined based on the unsharp masking, beta modeling and by the neural network.

Unsharp masking				Beta modeling			
Cavity number	R (kpc)	a (kpc)	b (kpc)	Cavity number	R (kpc)	a (kpc)	b (kpc)
1	4.76	2.36	1.07	1	6.44	2.46	2.08
2	3.99	3.00	2.08	2	7.64	3.74	2.13
3	1.23	0.56	0.52	3	3.93	2.50	2.14
4	0.57	0.37	0.22	4	3.74	1.91	0.83
5	0.67	0.33	0.26	5	3.27	1.76	1.50
6	3.63	1.81	1.14	6	3.89	1.53	0.63
7	3.24	1.64	1.39	7	2.00	0.99	0.87
8	7.48	3.73	2.56	8	0.93	0.54	0.44
9	6.43	2.45	1.99	9	1.15	0.33	0.28

Neural network			
Cavity	R (kpc)	a (kpc)	b (kpc)
N	3.59	2.97	2.78
S	3.97	3.88	2.77

Table 4.6: Parameters of the cavities depicted in fig. 4.19.

Method	Cavity	V (10^{59} m^3)	$E = 4pV$ (10^{56} erg)	t_{age} (Myr)	P_{jet} ($10^{42} \text{ erg s}^{-1}$)
UM	2	$19.5^{+1.3}_{-1.2}$	5.8 ± 0.4	9.76 ± 0.03	3.3 ± 0.9
	8	$37.0^{+2.0}_{-1.9}$	8.4 ± 0.4	18.39 ± 0.06	
Beta	2	$15.3^{+1.1}_{-1.0}$	4.6 ± 0.3	9.60 ± 0.03	2.6 ± 0.7
	8	$28.8^{+1.7}_{-1.6}$	6.5 ± 0.4	18.66 ± 0.07	
NN	N	29.1 ± 1.6	8.7 ± 0.5	8.78 ± 0.03	7.4 ± 1.3
	S	$37.0^{+2.2}_{-2.1}$	13.1 ± 0.7	9.70 ± 0.03	

Table 4.7: Derived quantities of the cavities depicted in fig. 4.19.

4.2.4 NGC 5813

NGC 5813 is the central galaxy of a group bearing the same name. Its diffuse gas has remarkably regular morphology with no clear signs of a recent merger event (Randall et al., 2015). A detailed study of this galaxy, its cavities and shock fronts is presented in Randall et al. (2015). Its distance was taken to be 32.2 Mpc (Tonry et al., 2001), giving scale of 156 pc per arcsec.

For input image creation, archival observations 12951, 12952, 12953, 13246, 13253 and 13255 were processed, adding up to ~ 455 ks deep image. While even more observations exist, they were not used since their influence on the combined image would be negligible for the purpose of the cavity detection. For all exposure corrections, monoenergetic 0.875 keV exposure maps were used. Individual observations were reprojected on ObsID 129553. The 0.5 – 2.0 keV energy range was used.

Cavity detection

The NGC 5813 X-ray emission clearly shows shock fronts surrounding the innermost two cavities as well as a more distant one created by the previous outburst. Here, only the two

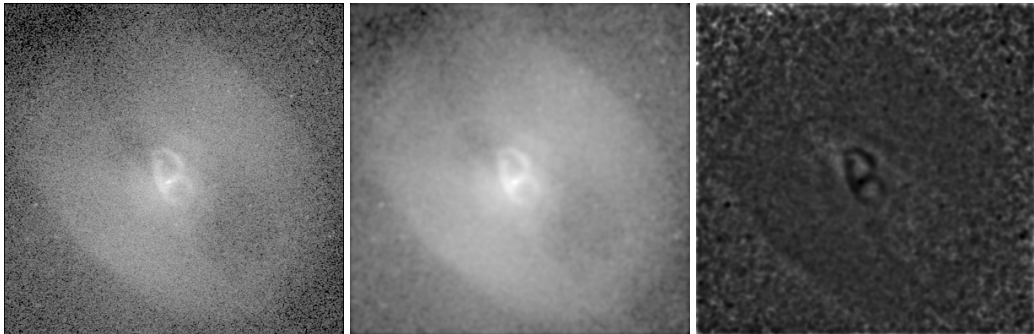


Figure 4.20: From left to right are presented the input image, the small (2) scale smoothed image and the unsharp masked image from smooth images with scales 10 and 2 sigma. All images of NGC 5813 are 192.7 arcsecs wide and 197.7 arcsecs high, corresponding to 30.1 x 30.8 kpc.

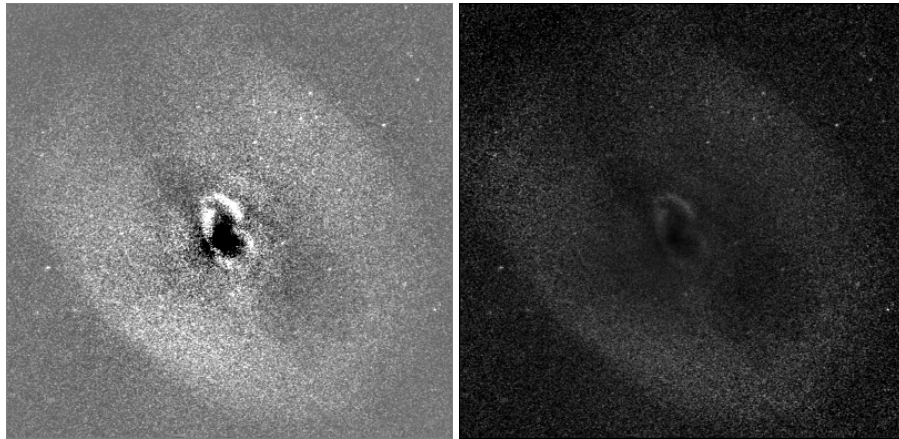


Figure 4.21: From left to right are presented the residual image and the normalized image based on the beta modeling.

youngest generations of bubbles were studied but the existence of third pair was confirmed as well by Randall et al. (2015).

Fig. 4.20 depicts the input image along with small (2) scale smooth image and a standard (scales 10 and 2) unsharped masked one. While the youngest pair of bubbles is very clearly visible, the edges of the southern outer one are less clear and for the northern they appear unclear. That is probably due to the leakage of the northern innermost cavity. Furthermore, the outer southern bubble appears remarkably circular as opposed to its northern counterpart.

The resulting images based on beta modeling are presented in fig. 4.21. However, the circular area surrounding the core and extending roughly twice the distance of the innermost cavity pair shows slight signs of oversubtraction. That is probably due to pronounced shock fronts which introduce significant departures from spherical symmetry. Nevertheless, the cavities are clearly visible.

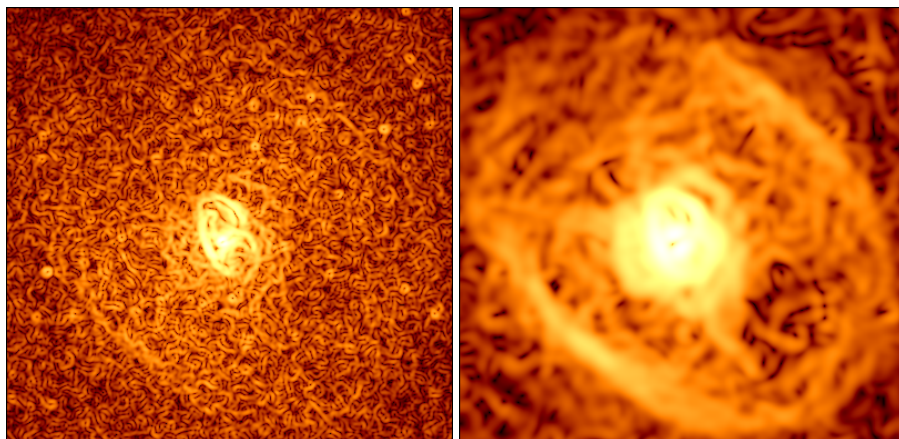


Figure 4.22: The GGM filtered images with sigma 2 and 6.

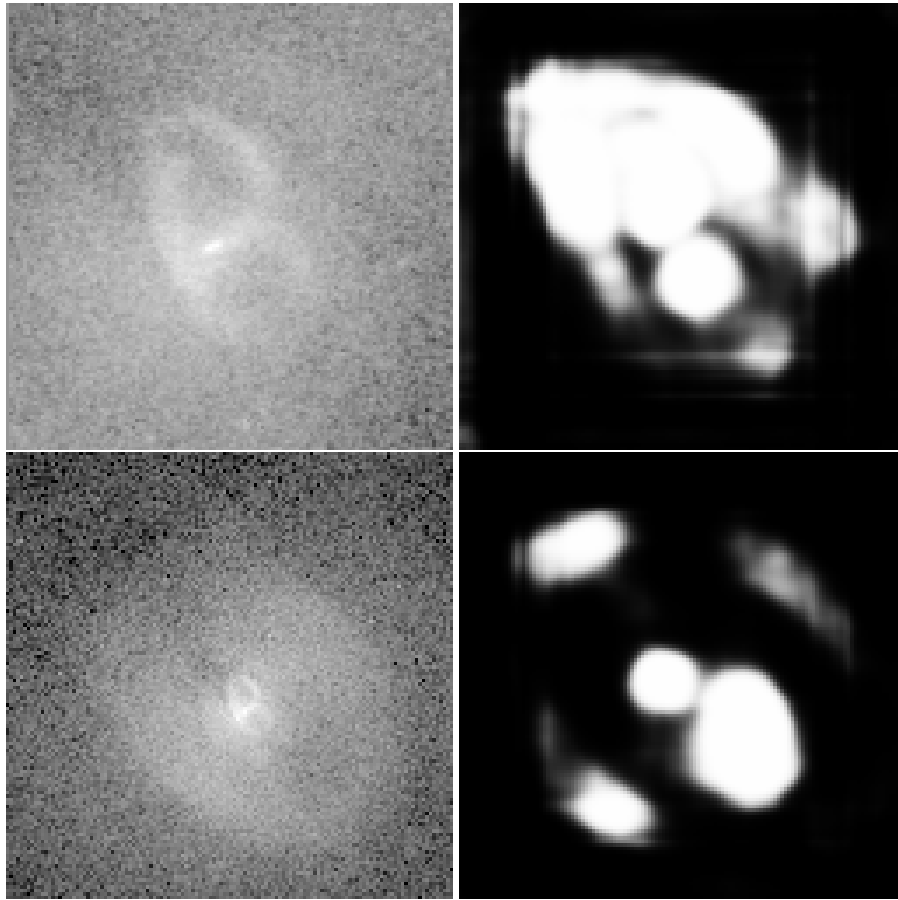


Figure 4.23: The input image and the resulting pixel-wise cavity prediction of the neural network for two differently sized images of NGC 5813. Higher values of cavity prediction denoted by white indicate high level of confidence that cavities are present. The sides of top images correspond to 9.8 kpc and of the bottom ones to 39.3 kpc.

Fig. 4.22 depicts the GGM filtered images. The left one with sigma of 2 nicely highlights the bright rims surrounding the innermost cavities. The right image with sigma 6 then shows the outer southern cavity. The opposing northern outer cavity is not visible in any of the GGM filtered images, probably due to having a far too low gradient.

Two different images of NGC 5813 were processed by the neural network for cavity detection. In fig. 4.23, the resulting cavity predictions for the inner and more distant pair of bubbles are presented. The network has not only detected the bubbles but also the shocks associated with similar surface brightness depressions. Compared to results of other imaging techniques, it can be seen that the network probably overestimated the bubble sizes.

The cavity sizes determined from the presented images are depicted in fig. 4.24. Their corresponding parameters are listed in tab. 4.8 and derived quantities follow in tab. 4.9.

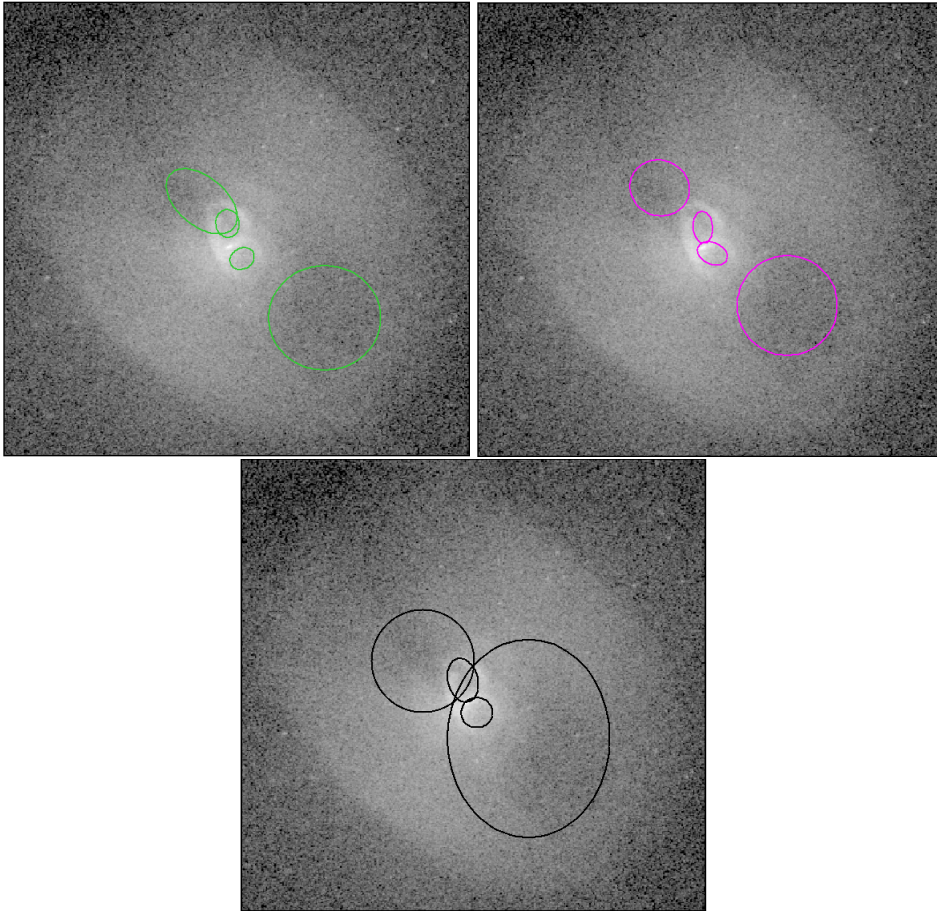


Figure 4.24: From left to right are presented the cavities identified from unsharp masking, beta modeling and by the neural network.

Unsharp masking				Beta modeling			
Cavity	R (kpc)	a (kpc)	b (kpc)	Cavity	R (kpc)	a (kpc)	b (kpc)
inner N	1.50	0.93	0.78	inner N	1.29	1.06	0.65
inner S	1.16	0.84	0.68	inner S	0.75	1.04	0.71
outer N	3.51	2.75	1.61	outer N	4.87	2.00	1.84
outer S	7.89	3.73	3.47	outer S	6.81	3.33	3.30

Neural network			
Cavity	R (kpc)	a (kpc)	b (kpc)
inner N	1.46	1.49	0.99
inner S	0.99	1.06	1.00
outer N	3.97	3.43	3.43
outer S	4.79	6.60	5.40

Table 4.8: Parameters of the cavities depicted in fig. 4.24.

Method	Cavity	V (10^{58} m^3)	$E = 4pV$ (10^{55} erg)	t_{age} (Myr)	P_{jet} ($10^{41} \text{ erg s}^{-1}$)
UM	inner N	$7.6^{+1.6}_{-1.3}$	$4.4^{+0.9}_{-0.8}$	3.43 ± 0.01	7.7 ± 1.0
	inner S	$5.4^{+1.3}_{-1.1}$	$3.1^{+0.7}_{-0.6}$	2.65 ± 0.01	
Beta	inner N	$7.2^{+1.6}_{-1.3}$	$4.1^{+0.9}_{-0.8}$	2.93 ± 0.01	13.0 ± 4.0
	inner S	$8.0^{+1.7}_{-1.4}$	$4.6^{+1.0}_{-0.8}$	1.71 ± 0.01	
NN	inner N	$22.4^{+3.3}_{-2.9}$	$12.8^{+1.9}_{-1.6}$	3.33 ± 0.01	23.0 ± 4.7
	inner S	$13.4^{+2.3}_{-2.0}$	$7.7^{+1.3}_{-1.1}$	2.25 ± 0.01	

Table 4.9: Derived quantities of the cavities depicted in fig. 4.24.

4.2.5 NGC 708 (A262)

NGC 708 is a BCG (the brightest cluster galaxy) at the centre of the Abell 262 galaxy cluster. Consequently, it is rather bright for its high distance which was taken to be 71 Mpc (Tully et al., 2013), corresponding to 344 pc per arcsec scale.

The input image is a courtesy of N. Werner. It was created from both available archival observations with ObsIDs 2215 and 7921. The approximate exposure is ~ 148 ks.

Cavity detection

In the central region of NGC 708 is rather unusual bright feature resembling a slated Z shape. The brightness quickly drops beyond the core making the cavity detection difficult especially in the case of the west bubble.

In fig. 4.25 is presented the input image along with the small (2) scale one and standard unsharp masked one (scales of 10 and 2). Whereas the east bubble is shown rather clearly, in a presumed place of the other one is present a series of dark circles.

The fitting with beta model reveals the east bubble rather clearly, even though signs of oversubtraction around the central region are present as well (see fig. 4.26). The extent of the other cavity is again rather dubious, although it is more visible than in the unsharped masked image. The GGM filtered image with extent of 4 sigma shows signs of the left cavity but not the other one. Instead, a tail-like feature is highlighted. The radio emission

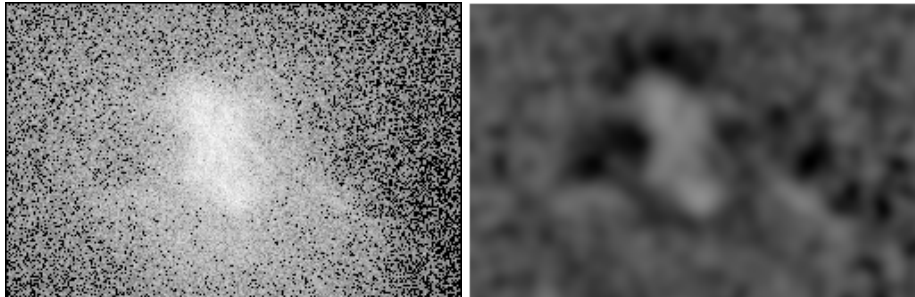


Figure 4.25: From left to right are presented the input image and the unsharp masked image from smooth images with scales 10 and 2. All images of NGC 708 are 125 x 81 arcsec, corresponding to 43.0 x 27.9 kpc.

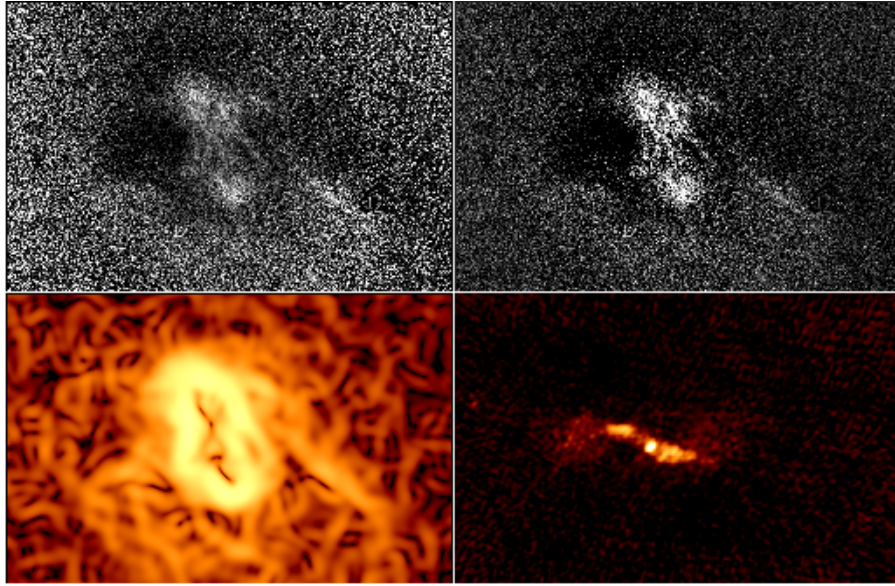


Figure 4.26: From left to right are presented the residual image and the normalized image based on the beta modeling, the GGM filtered image (4 sigma) and the 1.4 GHz radio emission.

shows both lobes nicely, but they appear significantly smaller than the X-ray cavities associated with them.

The cavity prediction of the neural network is presented in fig. 4.27. The network has detected regions very similar to beta residuals, including the top region above the core, which was not interpreted as cavity in any of the images. Nevertheless, it is associated with surface brightness depression comparable in magnitude to the cavities and thus its detection is not surprising.

In fig. 4.28, the estimated cavity sizes are presented, each overlaid over the input image. The parameters of the cavities are presented in tab. 4.10.

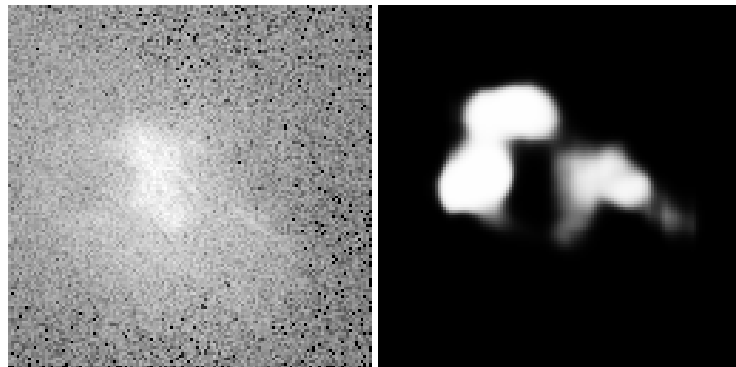


Figure 4.27: The input image and the resulting pixel-wise cavity prediction of the neural network. Higher values denoted by white indicate high level of confidence that cavities are present. Sides of both images correspond to 43.3 kpc.

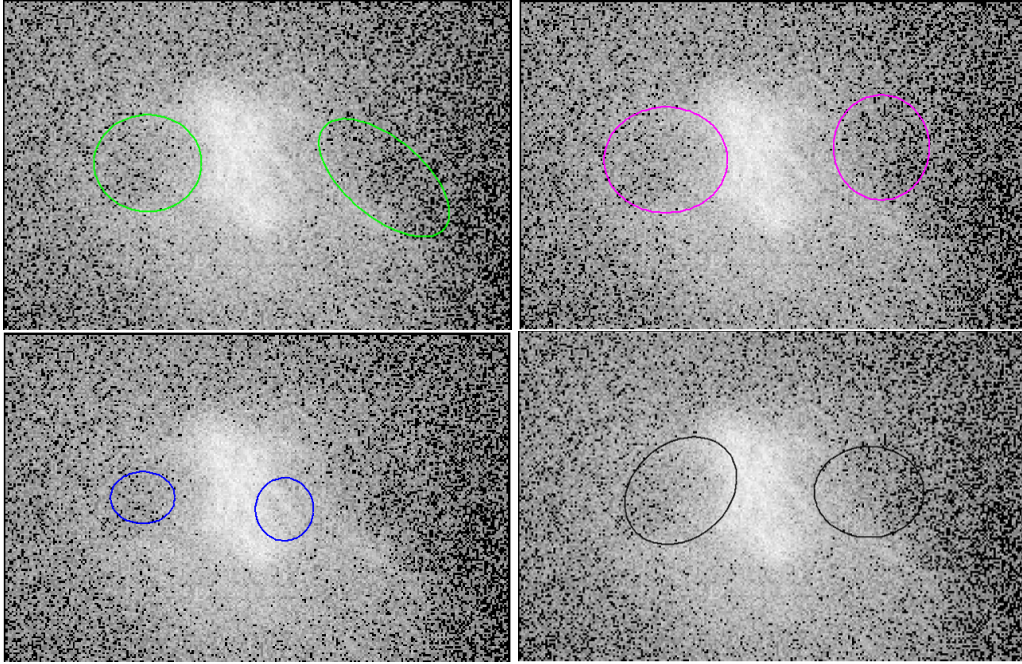


Figure 4.28: From left to right are presented the cavities as they were determined based on the unsharp masking, beta modeling, 1.4 GHz radio emission and by the neural network.

Method	R (kpc)	a (kpc)	b (kpc)	V (10^{60} m^3)	$E = 4pV$ (10^{57} erg)	t_{age} (Myr)	P_{jet} ($10^{42} \text{ erg s}^{-1}$)
UM	7.88	4.59	4.12	$10.1^{+0.9}_{-0.8}$	3.9 ± 0.3	15.6 ± 0.1	13.1 ± 4.5
	12.4	6.71	3.32	13.7 ± 1.1	4.0 ± 0.3	24.5 ± 0.2	
Beta	7.69	5.29	4.51	$14.4^{+1.1}_{-1.0}$	5.6 ± 0.4	15.2 ± 0.1	15.8 ± 1.5
	10.8	4.45	4.10	9.7 ± 0.8	2.8 ± 0.2	21.4 ± 0.1	
Radio	8.34	2.75	2.21	1.9 ± 0.3	0.7 ± 0.1	16.5 ± 0.1	5.8 ± 0.7
	4.10	2.69	2.47	2.1 ± 0.3	$1.1^{+0.2}_{-0.1}$	8.12 ± 0.05	
NN	6.34	5.19	4.06	$12.0^{+1.0}_{-0.9}$	4.7 ± 0.4	12.56 ± 0.08	17.9 ± 2.8
	9.65	4.65	3.86	9.4 ± 0.8	3.7 ± 0.3	19.1 ± 0.1	

Table 4.10: Parameters of the cavities depicted in fig. 4.28. First is listed the western (left) cavity.

Chapter 5

Discussion

This chapter encapsulates the results presented in the previous one and discusses their implications. Firstly, the consequences of using different imaging techniques used for cavity detection on derived volumes are summarized. Then, other sources of uncertainties affecting the determination of jet powers which were examined are stated along with the magnitude of their influence. The chapter concludes with the overview of the performance of the neural network and discusses its suitability for the cavity detection task and possibilities of future improvements.

5.1 Imaging techniques and their influence on derived cavity volumes

Three different imaging techniques were used for cavity detection – the unsharp masking, beta model and radio contours. Furthermore, a new method of using a neural network for cavity detection was tried out. Results of this method are discussed in sec. 5.4.

For each detection method, the corresponding cavity volumes were derived independently and are presented in fig. 5.1. For the purpose of comparison of the different techniques only, the derived volumes were divided by their mean value. The influence of physical distance of the galaxies as well as other uncertainties discussed further in the following section was thus effectively removed from the plot.

In the figure, it can be clearly seen that even when different techniques are used for cavity detection, the derived volumes agree with each other well within the order of magnitude. Nevertheless, it is clear that the values differ far more than the propagated uncertainties which were associated with them. This is probably a consequence of a number of reasons presented in the next paragraphs.

While the unsharp masking has the undeniable advantage of using the original data without the need of making assumption about the geometry of the galaxy, it presents

5.1. Imaging techniques and their influence on derived cavity volumes

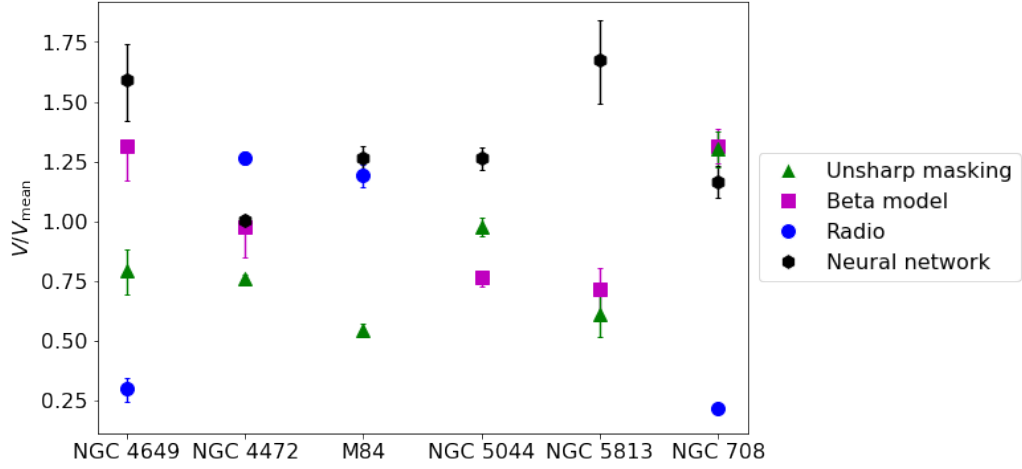


Figure 5.1: The summed volumes of the cavity pairs presented in the previous chapter. The values were divided by the mean value for each galaxy in order to judge the influence of the different techniques of detection on their own.

drawbacks as well. Mainly, it can be rather unreliable since it highly depends on the subjective choice of the smoothing scales. As a result, the true size of the cavities cannot be determined from unsharp masked image, since the size of the cavities in the image vary with the choice of the smoothing scales. Generally, the smaller scales ought to be preferred since they deform the original sizes the least. However, that may not be an option in case the observation is not sufficiently deep.

On the other hand, the beta model does not suffer from this deficit since it does not involve smoothing of the image. However, it requires the assumption of spherical symmetry. Thus, while it can describe spherically symmetrical objects it cannot be used for highly asymmetrical objects. Also, in case of insufficiently deep observations, there may be too few photons to obtain a statistically acceptable value of the minimization function of the fit.

Furthermore, it is worth noting that even rather spherically symmetrical galaxies for which a statistically good fit is obtained can show questionable residuals which does not seem to be associated with real features. That is probably because the model is not a physical one and thus cannot describe more complicated regions (especially near the core) sufficiently well. Moreover, a projected surface brightness profile is fitted which can give biased results. Troublesome is that the residuals of the fit, or in other words, departures from spherical symmetry can be created in various ways, as was discussed in sec. 4.1.2 (e.g. gas sloshing or asymmetrical geometry). Nevertheless, the beta model can more clearly show the extent of the cavities than raw image, in which the outer edges of the cavities are often not clearly visible. Thus while the beta model ought not be used to judge the presence of the cavities on its own, the physical nature of the residuals can be confirmed when it is used in combination with other techniques.

The biggest issue concerning the radio emission is its unclear relation to the X-ray cavities. While it is not surprising to find radio emission at the location of the cavities, it

is also not uncommon not to detect it (e.g. NGC 5044). Furthermore, in some cases, the radio emitting plasma can be observed to be leaking out as in case of M84. Moreover, the radio emission can be misplaced with relation to the absence of the X-ray radiation or the detected X-ray cavities can appear significantly smaller than the associated radio source (Nulsen et al., 2009) or the other way round. Further dubious also remains the determination of the bubble edges in it, since it is unclear what frequency ought to be considered the lowest one associated with the bubbles. As a result, this method tends to give most greatly varying results, as will be further discussed in section 5.3.

Furthermore, the GGM filtered images were presented, since they highlight gradients in the images. Nevertheless, the gradients associated with the cavities tend to be too small in most cases for them to be detected in the GGM filtered images. Thus, the GGM filtering seems more suitable for e.g. judging gas motions of the ISM which can bend the cavity shapes rather than for cavity detection itself.

In conclusion, while the systematic uncertainty associated with the use of different detection techniques is far greater than the uncertainty stemming from different assumption about the cavity shapes (prolate or oblate), it seems constrained within a factor of few.

5.2 Systematic uncertainties associated with the deprojected profiles

Since the systematic uncertainties are generally substantially larger than the statistical ones, some of them were studied in greater detail. The full investigation of them is beyond the scope of this work, but the following paragraphs give an estimate of their magnitude.

5.2.1 Anti-correlation of metallicity and normalization

For deprojection of the spectra, the abundances had to be frozen because the metallicity profile was widely oscillating otherwise and at some annuli, gaining unphysical values. Even though the values of the metallicities itself are not important for this analysis, this is of importance because there exist a strong anti-correlation of metallicity and normalization.¹ This has been investigated using the projected profiles. In fig. 5.2 is a contour plot showing this anti-correlation for one of the outer annuli, where the best fit profiles of normalization and metallicity appear more or less monotone.

However, when the values of metallicities are frozen as is the case with deprojected profiles, such a plot cannot be produced and therefore corresponding systematic uncertainty cannot be accurately estimated. Nevertheless, through conducting fits with different values of metallicities, it has been observed that the values of normalization are not greatly influenced as long as relatively monotone profile of metallicity is assumed. The values of metallicity used here were adapted from projected fits of Mernier et al. (2017). They were obtained from analysis data with SPEX version 2.05 from MOS and pn XMM-Newton instruments in 0.5 – 10 keV and 0.6 – 10 keV respectively. These instruments are known

¹Throughout this text, normalization is used as a synonym of the emission measure. All the metallicity values are reported with respect to proto-solar abundances of Lodders et al. (2009).

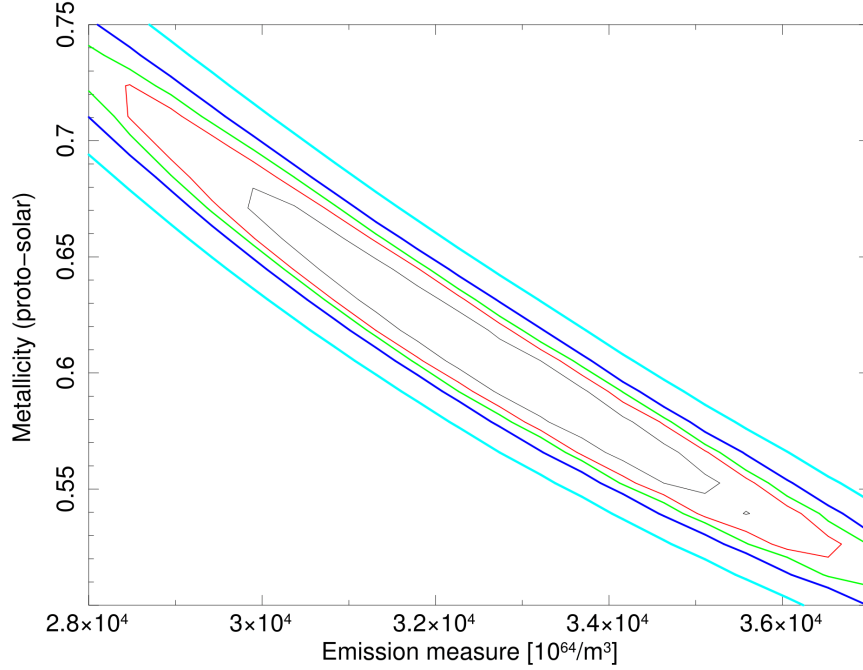


Figure 5.2: Contour plot in parameter space showing anti-correlation between metallicity and normalization in one of the outer annuli of the fit of projected values. The contours correspond to the 68.3%, 90%, 95.4%, 99% and 99.99% confidences.

to have better spectral resolution than Chandra. As a result, anti-correlation of these values with normalization are weaker. Nevertheless, they are still present, as can be seen in fig. 5.3. These values are in agreement with those obtained in this analysis while fitting the projected data with SPEX software package. However, values obtained with the XSPEC show systematic offset corresponding to $\sim 8\%$ (higher at innermost annuli), most likely due to the different plasma codes implemented. This ought not to have great influence on our analysis since the trends of the profiles are in agreement. For details, see 5.2.2.

The best fit deprojected metallicity profile is oscillating more widely than the projected one, but on average seems to be in agreement with the values obtained for the projected profiles. Thus, the adaptation of projected values of metallicity of Mernier et al. (2017) seems appropriate. Nevertheless, the results ought to be interpreted with care, bearing in mind that the systematic uncertainty associated with the anti-correlation of metallicity and normalization which cannot be accurately estimated is most likely substantially higher than the statistical uncertainties given by the error bars in the plots. Also if the assumption of the monotone metallicity profile is not appropriate, the results of the fitting might be misleading as well. Furthermore, it should be noted that the models which were used are rather simplistic, assuming only one temperature plasma. However, this assumption is unlikely to hold true. It is more probable that in reality the plasma is multi-temperature with temperatures of most of the particles being close to the one found from the fit. If this

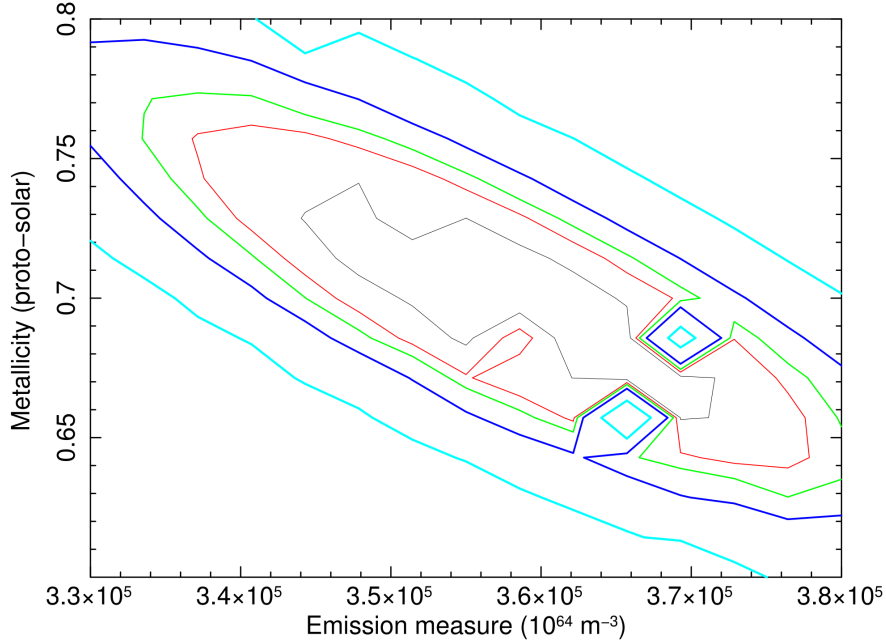


Figure 5.3: Contour plot in parameter space showing anti-correlation between metallicity and normalization of the fit by Mernier et al. (2017) from which were the abundance value adapted for deprojection in this work. The contours correspond to the 68.3%, 90%, 95.4%, 99% and 99.99% confidences.

holds true, the spectral lines would be broadened and thus it would be harder to distinguish one from another. This, together with the limited spectral resolution could explain why the discovered anti-correlation is so strong.

5.2.2 Choice of the fitting range

Since most of the emission of NGC 4649 is in the soft band (< 2.5 keV), it is desirable to fit the data from the lowest energy possible. However, due to calibration issues, the recommended fitting range is from 0.7 keV. Nevertheless, it is generally believed that the data in the 0.6-0.7 keV range are sufficiently well calibrated to be used. In order to investigate this, the projected profiles were fitted in the 0.6-2.5 keV range as well as in the 0.7-2.5 keV range. In the fig. 5.4 below, the abundance profiles of the projected fits are shown. It can be observed that the systematic offset caused by the choice of fitting range is comparable in size to the offset caused by the use of different plasma codes. However, since the trends of the profiles in both energy ranges are same, we believe that the 0.6-0.7 keV range is indeed sufficiently well calibrated and therefore is safe to use. Also, based on the comparison with Mernier et al. (2017), the values from the fits in the 0.6-2.5 keV range may be closer to reality as a result of using more data. The upper limit of 2.5 keV was chosen based on the visual examination of the data, which showed that the emission of NGC 4649 in the energy range over 2.5 keV is very low. Furthermore, since the magnitude of the systematic offset caused by the use of different fitting range is roughly two times the

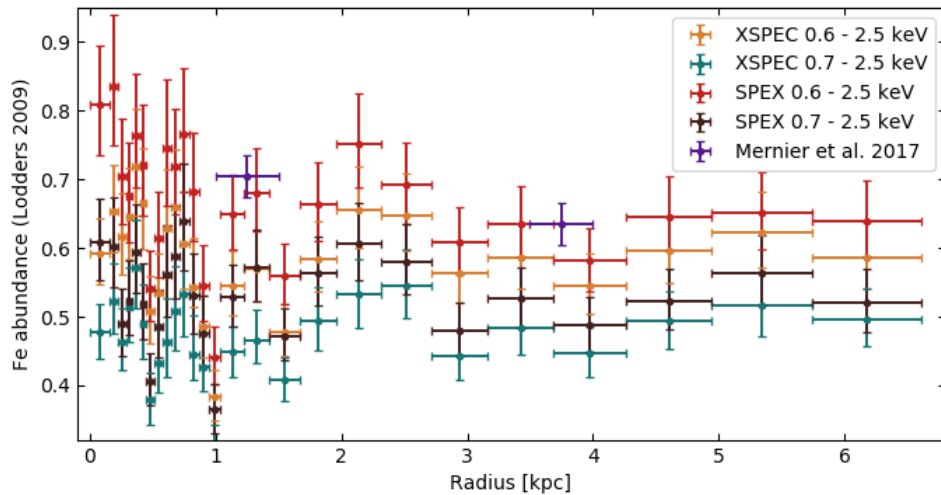


Figure 5.4: Comparison of abundance profiles of the projected fits. While the offset between XSPEC and SPEX profiles most likely stems from systematic uncertainty associated with the use of different plasma codes, the origin of the offset caused by a different fitting range is unclear.

one sigma errors for the projected fits, it would seem that one ought to be very careful and investigate how much are they influenced by the choice of the fitting range.

5.3 Power of the jets

The determination of jet powers is affected by a number of uncertainties. The influence of using different techniques for determination of the cavity sizes was already discussed in sec. 5.1. The impact of systematic uncertainties associated with the spectral fitting were indicated in sec. 5.2. However, there are other sources of uncertainties worth considering.

In fig. 5.5 are plotted summed powers of jets for each imaging technique along with values from literature. The galaxies are arranged by their physical distances in order to investigate the magnitude of the error associated with it. Since the galaxies which are further out are angularly smaller, the error of determining the bubble size could be expected to grow bigger with the galaxy distance since it propagates into a larger physical size. However, in the plot, it can be seen that this source of error has to be substantially smaller than the other ones, since a trend of increasing scatter of values with distance is not apparent.

Nevertheless, it is clear that the scatter of jet powers can be up to an order of magnitude which is substantially higher than the commonly assumed a factor of two (Allen et al., 2006) or a factor of a few (Randall et al., 2015) stemming from the assumption of different timescales. In the case of NGC 4649 and M84, the differences between the presented values and those from the literature stem mainly from the use of radio data. Since the determination of the cavity extent in radio emission can largely differ from its X-ray

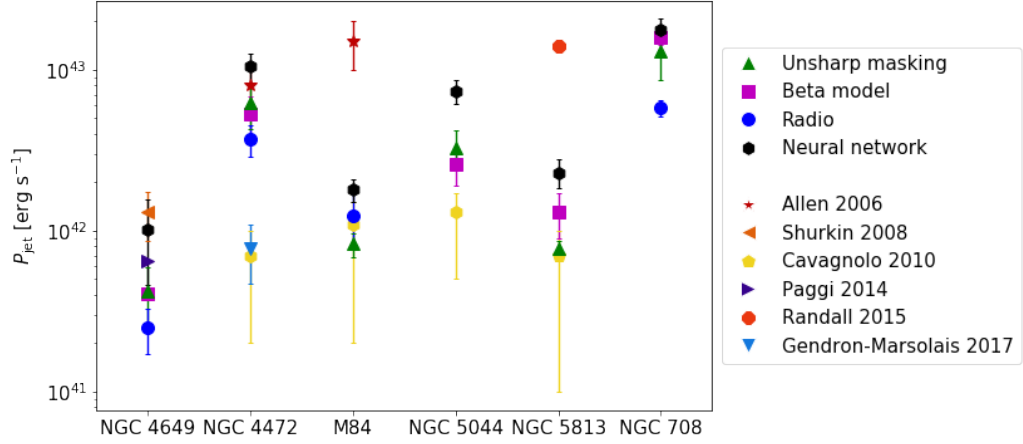


Figure 5.5: The power of the jets derived from volumes presented in the previous section. Compare with values from literature, where Allen et al. (2006) and Shurkin et al. (2008) relied mainly on radio emission, Paggi et al. (2014) and Gendron-Marsolais et al. (2017) on beta modeling and rest of the authors on combination of techniques employed on X-ray data. The galaxies are arranged by their distance.

counterpart (see sec. 5.1). In the case of M84, it was also observed that the radio emitting plasma leaks out of the ISM (Finoguenov et al., 2008) and based on the radio emission alone, it cannot be distinguished whether the scenario of two generation of bubbles or only one ought to be considered, resulting in the order of magnitude higher value from Allen et al. (2006). Similarly, in case of NGC 4472, the order of magnitude difference is caused by different interpretation of the same data, although in this instance, only X-ray data were considered. This is apparent from comparison of figures 4.10 and 4.11. In case of NGC 5044, the geometry is also questionable. Since it posses high number of cavities, it is not clear which originated from the same outburst. Furthermore, a substantial difference can also be caused by making an inappropriate assumption as is the case of NGC 5813. This galaxy has pronounced shocks into which was deposited a comparable amount of energy as is the amount of cavities internal energy. Consequently, the assumption that the energy deposited in the form of shocks is negligible which was used here is not justified and the value from Randall et al. (2015) is more likely correct.

In fig. 5.6, we plot Bondi powers adapted from Russell et al. (2013) (except for NGC 4649) as a function of jet power. For comparison are also presented the values from Allen et al. (2006) and Russell et al. (2013) where powers of the jets were adapted from Cavagnolo et al. (2010).

In Allen et al. (2006), based on the powers determined mainly from radio data, a log-log correlation between the Bondi accretion power and power of the jets was proposed. However, when values only from Russell et al. (2013) are considered, this relation is becoming less apparent. This is among other things a consequence of a significant difference in cavity powers determined for some of the objects which were studied by both authors. Furthermore, upon viewing the amount of scatter caused by the uncertainty of the jet

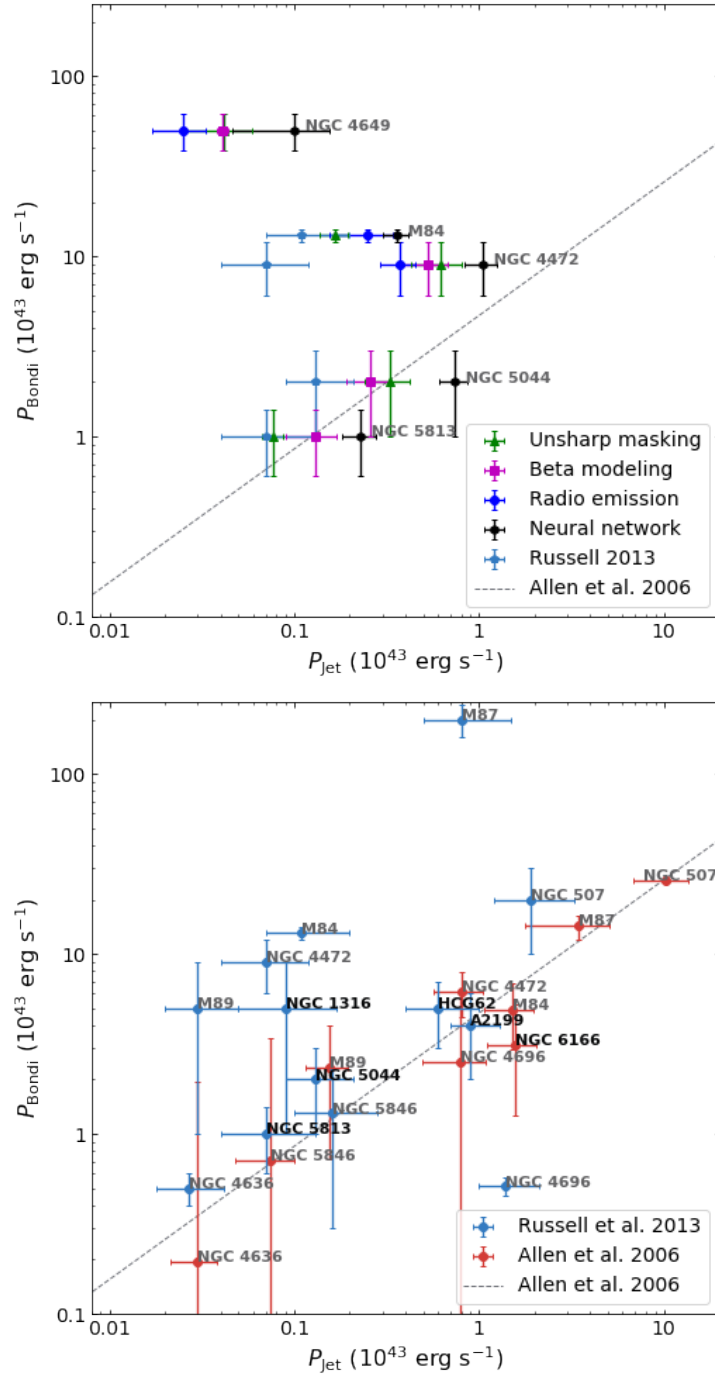


Figure 5.6: In top figure are the Bondi powers adapted from Russell et al. (2013) (except for NGC 4649) plotted as a function of jet powers determined in this thesis. For comparison, values from Allen et al. (2006) and Russell et al. (2013) are plotted in the bottom graph. All the objects which were studied by both authors have grey labels while those studied only in one work have black labels. From comparison of jet powers from literature and this work, it is clear that the scatter present in them is far too large to constrain the relation between Bondi accretion and jet powers and consequently, better understand the AGN feedback cycle.

powers in this work, it is clear that tighter constraints need to be placed on these errors before the relation between Bondi power and jet power can be studied and consequently, the AGN feedback better understood.

5.4 The use of neural networks for cavity detection

Here, for the first time, we report a successful application of convolutional neural network for the task of cavity detection in images of real galaxies. While it has some limitations, these can be further improved upon and the network has demonstrated remarkable ability to generalize and predict cavities in galaxies whose morphology is far more complex than those which were created for the training dataset.

First of all, the degree of generalization the network has achieved is remarkable. While it was presented with the task of cavity detection on the training dataset which included mostly images with two opposing bubbles or none, it learned to detect gradients in the images without any prejudice concerning their shapes and locations. In fig. 5.7 is presented the core region of M87 and the corresponding cavity prediction. It is clear that even though the morphology in this image is far more complex than that in all of the images on which the network was trained, the network detected various surface brightness depressions associated with the cavities as well as shocks.

Upon comparing the cavity predictions for the galaxies in chap. 4 to other detection methods presented, it can be seen that the output of the network seems most in agreement with the results of the beta modeling. This is perhaps not surprising, since the network was trained on galaxies modeled with either beta or double beta model. Thus, it was tasked with searching for departures from these profiles which is essentially what can be seen in the residual and normalized images.

From comparison of the volumes in fig. 5.1 and powers in fig. 5.5, it seems that the network in general tends to overestimate the sizes of the bubbles in real galaxies. This is most likely a consequence of a bias present in the network in terms of the magnitude of the values in the input images. When the network is presented with images with higher number of counts, it tends to detect the cavities with substantially higher confidence and their spatial extent is larger. On the other hand, when the same image with values divided by small whole number constants are presented, the cavities are detected with substantially lower confidence and are smaller as well. This is probably a result of bias present in the training dataset. Since the depth of the cavities was scaled relatively to the magnitude of the emission at their location, they were more easily detectable in brighter systems with higher count values. As a result, the network learned to detect the bubbles with higher confidence in these. Thus, the confidence of the detected cavities and their spatial extent is scaled relative to the brightness of the input image rather than representing the true probability of the cavity detection.

Nonetheless, when images with far too high values are presented, the cavities in them tend to be detected with low confidence and spatially smaller as well. Therefore, it seems that even though the network has forms of regularization through the batch normalizations, it is highly sensitive to the normalization of the input images. Nevertheless, this issue ought

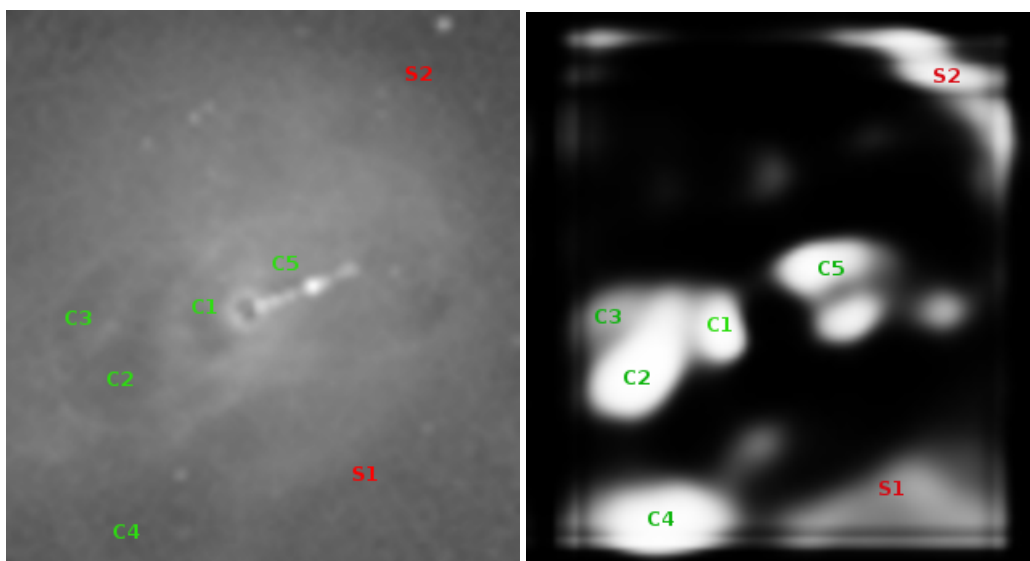


Figure 5.7: The input image and resulting pixel-wise cavity prediction of the core region of M87. Higher values in the predicted image on right denoted by white indicate high level of confidence that cavities are present. Even though the morphology of the galaxy is far more complex than those in the images on which the network was trained, the network was able to generalize well. Thus, it detects shocks (marked in red) as well as cavities (marked in green), since they are associated with similar surface brightness depressions. (The left image is a courtesy of N. Werner.)

to be resolved by retraining it on a dataset with a more tightly constrained normalization of the input images.

To summarize, the network learned to generalize remarkably well to galaxies with more complex morphologies and detects not only cavities but also shocks which are associated with similar surface brightness depressions. However, it is highly sensitive to a range in which lies most of the values in the input image. Upon deviation from the optimal one to either side, the predicted cavities tend to get smaller and are detected with significantly lower confidence. Thus, the predicted values cannot be interpreted as probabilities at present. Nevertheless, this issue ought to be resolved by placing tighter constraints on the normalization of the input images. Consequently, the network will be then capable of automatizing the cavity detection with precision rivalling that of the experienced astronomers.

Conclusions and future outlook

Jet powers of a sample of nearby elliptical galaxies were estimated. By employing various imaging techniques, derived cavity volumes were studied. The errors this introduced to jet powers as well as other sources of uncertainties were examined. It was discovered that:

- Upon using various techniques for cavity detection, the differences in estimated jet powers are greater than propagated errors. However, they are constrained within a factor of five.
- From comparison with literature, over an order of magnitude differences in jet powers were found. The largest errors are stemming from use of radio data and different interpretations of the same data.
- The uncertainty of jet powers are too large at present for a conclusive study of the AGN feedback cycle. Thus a neural network was proposed for an objective cavity detection.
- The neural network was able to generalize to more complex morphologies remarkably well, being able to detect cavities as well as shocks. Although it tends to overestimate the cavity sizes and due to incorrect normalization of the input images the output values cannot be interpreted as probabilities at present, this can be corrected.
- In future work, the network will be retrained on improved dataset, various input normalizations (stretch functions) will be tried out and mechanisms for automated extraction of the cavity positions and sizes added. Consequently, it will be able to objectively estimate cavity sizes and thus better constrain the values of jet powers.

Bibliography

- Allen, S. W., Dunn, R. J. H., Fabian, A. C., Taylor, G. B., and Reynolds, C. S. (2006). The relation between accretion rate and jet power in X-ray luminous elliptical galaxies. *Monthly Notices of the Royal Astronomical Society*, 372(1):21–30.
- Arnaud, K. A. (1996). XSPEC: The first ten years. *Astronomical Data Analysis Software and Systems*.
- Arnaud, K. A., Smith, R. K., and Siemiginowska, A. (2011). *Handbook of x-ray astronomy*. University Press.
- Balucinska-Church, M. and McCammon, D. (1992). Photoelectric absorption cross sections with variable abundances. *The Astrophysical Journal*, 400:699–700.
- Birzan, L., Rafferty, D. A., McNamara, B. R., Wise, M. W., and Nulsen, P. E. J. (2004). A Systematic Study of Radio-induced X-Ray Cavities in Clusters, Groups, and Galaxies. *The Astrophysical Journal*, 607(2):800–809.
- Blakeslee, J. P., Jordán, A., Mei, S., Côté, P., Ferrarese, L., Infante, L., Peng, E. W., Tonry, J. L., and West, M. J. (2009). the Acs Fornax Cluster Survey. V. Measurement and Recalibration of Surface Brightness Fluctuations and a Precise Value of the Fornax-Virgo Relative Distance. *The Astrophysical Journal*, 694(1):556–572.
- Bondi, H. (1952). On spherically symmetrical accretion. *Monthly Notices of the Royal Astronomical Society*, 112:195.
- Brüggen, M., Scannapieco, E., and Heinz, S. (2009). Evolution of X-ray cavities. *Monthly Notices of the Royal Astronomical Society*, 395(4):2210–2220.
- Cash, W. (1979). Parameter estimation in astronomy through application of the likelihood ratio. *The Astrophysical Journal*, 228:939–947.
- Cavagnolo, K. W., Mcnamara, B. R., Nulsen, P. E. J., Carilli, C. L., and Jones, C. (2010). A relationship between agn jet power and radio power. *The Astrophysical Journal*, pages 1066–1072.

- Cavaliere, A. and Fusco-Fermiano, R. (1976). X-rays from Hot plasma in clusters of galaxies. *Physica Scripta*, 1976(49):137–144.
- David, L. P., Lim, J., Forman, W., Vrtillek, J., Combes, F., Salome, P., Edge, A., Hamer, S., Jones, C., Sun, M., O’Sullivan, E., Gastaldello, F., Bardelli, S., Temi, P., Schmitt, H., Ohyama, Y., Mathews, W., Brighenti, F., Giacintucci, S., and Trung, D. V. (2014). Molecular gas in the x-ray bright group NGC 5044 as revealed by Alma. *Astrophysical Journal*, 792(2).
- Diehl, S., Li, H., Fryer, C., and Rafferty, D. (2008). Constraining the Nature of X-ray Cavities in Clusters and Galaxies. *The Astrophysical Journal*, 687:173–292.
- Diehl, S. and Statler, T. S. (2007). The Hot Interstellar Medium of Normal Elliptical Galaxies. I. A Chandra Gas Gallery and Comparison of X-Ray and Optical Morphology. *The Astrophysical Journal*, 668(1):150–167.
- Dong, R., Rasmussen, J., and Mulchaey, J. S. (2010). A systematic search for X-ray cavities in the hot gas of galaxy groups. *Astrophysical Journal*, 712(2):883–900.
- Dunn, R. J., Allen, W., Taylor, G. B., Shurkin, K. F., Gentile, G., Fabian, A. C., and Reynolds, C. S. (2010). The radio properties of a complete, X-ray selected sample of nearby, massive elliptical galaxies. *Monthly Notices of the Royal Astronomical Society*, 404(1):180–197.
- Eckert, D., Ettori, S., Coupon, J., Gastaldello, F., Pierre, M., Melin, J. B., Brun, A. M. C. L., McCarthy, I. G., Adami, C., Chiappetti, L., Faccioli, L., Giles, P., Lavoie, S., Lefevre, J. P., Lieu, M., Mantz, A., Maughan, B., McGee, S., Pacaud, F., Paltani, S., Sadibekova, T., Smith, G. P., and Ziparo, F. (2016). The XXL Survey. XIII. Baryon content of the bright cluster sample. *Astronomy & Astrophysics*, 592:1–19.
- Fabian, A. C., Sanders, J. S., Allen, S. W., Crawford, C. S., Iwasawa, K., Johnstone, R. M., Schmidt, R. W., and Taylor, G. B. (2003). A deep Chandra observation of the Perseus cluster: shocks and ripples. *Monthly Notices of the Royal Astronomical Society*, 344:L43–L47.
- Finoguenov, A., Ruszkowski, M., Jones, C., Brueggen, M., Vikhlinin, A., and Mandel, E. (2008). In-depth Chandra study of the AGN feedback in Virgo elliptical galaxy M84. *The Astrophysical Journal*, 686:911–917.
- Fort, S. (2017). Towards understanding feedback from supermassive black holes using convolutional neural networks. *arXiv e-prints*.
- Garmire, G. P., Bautz, M. W., Ford, P. G., Nousek, J. A., and Ricker, Jr., G. R. (2003). Advanced CCD imaging spectrometer (ACIS) instrument on the Chandra X-ray Observatory. *Proceedings of the SPIE*, 4851:28–44.
- Gendron-Marsolais, M., Kraft, R. P., Bogdan, A., Hlavacek-Larrondo, J., Forman, W. R., Jones, C., Su, Y., Nulsen, P., Randall, S. W., and Roediger, E. (2017). Uplift, feedback and buoyancy: radio lobe dynamics in NGC 4472. *The Astrophysical Journal*, 848(1).

- Guo, F. (2015). The shape of X-ray cavities in galaxy clusters: Probing jet properties and viscosity. *Astrophysical Journal*, 803(1):48.
- Ioffe, S. and Szegedy, C. (2015). Batch Normalization: Accelerating Deep Network Training by Reducing Internal Covariate Shift. *arXiv e-prints*.
- Joseph, T. D., Maccarone, T. J., Kraft, R. P., and Sivakoff, G. R. (2017). A deeper look at the X-ray point source population of NGC 4472. *Monthly Notices of the Royal Astronomical Society*, 470(4):4133–4144.
- Kaastra, J. S., Mewe, R., and Nieuwenhuijzen, H. (1996). SPEX: a new code for spectral analysis of X & UV spectra. In Yamashita, K. and Watanabe, T., editors, *UV and X-ray Spectroscopy of Astrophysical and Laboratory Plasmas*, pages 411–414.
- Kalberla, P. M. W., Burton, W. B., Hartmann, D., Arnal, E. M., Bajaja, E., Morras, R., and Pöppel, W. G. L. (2005). The Leiden/Argentine/Bonn (LAB) Survey of Galactic HI. Final data release of the combined LDS and IAR surveys with improved stray-radiation corrections. *The Astronomy & Astrophysical Journal*, 440:775–782.
- Kormendy, J., Fisher, D. B., Cornell, M. E., and Bender, R. (2009). Structure and formation of elliptical and spheroidal galaxies. *Astrophysical Journal, Supplement Series*, 182(1):216–309.
- Krizhevsky, A., Sutskever, I., and Hinton, G. (2012). ImageNet Classification with Deep Convolutional Neural Networks. *Advances in Neural Information Processing Systems 25 (NIPS'2012)*, pages 1–9.
- Lodders, K., Palme, H., and Gail, H.-P. (2009). Abundances of the Elements in the Solar System. *Landolt Börnstein*.
- Longair, M. S. (2011). *High energy astrophysics*. Cambridge University Press.
- McNamara, B. R. and Nulsen, P. E. (2012). Mechanical feedback from active galactic nuclei in galaxies, groups and clusters. *New Journal of Physics*, 14.
- McNamara, B. R. and Nulsen, P. E. J. (2007). Heating Hot Atmospheres with Active Galactic Nuclei. *Annual Review of Astronomy & Astrophysics*, 45(1):117–175.
- Mernier, F., de Plaa, J., Kaastra, J. S., Zhang, Y.-Y., Akamatsu, H., Gu, L., Kosec, P., Mao, J., Pinto, C., Reiprich, T. H., Sanders, J. S., Simionescu, A., and Werner, N. (2017). Radial metal abundance profiles in the intra-cluster medium of cool-core galaxy clusters, groups, and ellipticals. *Astronomy & Astrophysics*, 603:A80.
- Nakahara, S., Hada, K., Honma, M., and Nakanishi, H. (2014). Multi-epoch, quasi-simultaneous 22/43 GHz observations of the M84 nucleus with VERA. *Proceedings of Science*, pages 3–6.

- Nulsen, P., Jones, C., Forman, W., Churazov, E., McNamara, B., David, L., and Murray, S. (2009). Radio mode outbursts in giant elliptical galaxies. *AIP Conference Proceedings*, 1201:198–201.
- Paggi, A., Fabbiano, G., Kim, D. W., Pellegrini, S., Civano, F., Strader, J., and Luo, B. (2014). Active galactic nucleus feedback in the hot halo of NGC 4649. *Astrophysical Journal*, 787(2):1–23.
- Panagoulia, E. K., Fabian, A. C., Sanders, J. S., and Hlavacek-Larrondo, J. (2014). A volume-limited sample of X-ray galaxy groups and clusters - II. X-ray cavity dynamics. *Monthly Notices of the Royal Astronomical Society*, 444(2):1236–1259.
- Randall, S. W., Forman, W. R., Giacintucci, S., Nulsen, P. E., Sun, M., Jones, C., Churazov, E., David, L. P., Kraft, R., Donahue, M., Blanton, E. L., Simionescu, A., and Werner, N. (2011). Shocks and cavities from multiple outbursts in the galaxy group NGC 5813: A window to active galactic nucleus feedback. *Astrophysical Journal*, 726(2).
- Randall, S. W., Nulsen, P. E., Jones, C., Forman, W. R., Bulbul, E., Clarke, T. E., Kraft, R., Blanton, E. L., David, L., Werner, N., Sun, M., Donahue, M., Giacintucci, S., and Simionescu, A. (2015). A very deep chandra observation of the galaxy group NGC 5813: AGN shocks, feedback, and outburst history. *Astrophysical Journal*, 805(2).
- Russell, H. R., Mcnamara, B. R., Edge, A. C., Hogan, M. T., Main, R. A., and Vantyghem, A. N. (2013). Radiative efficiency, variability and Bondi accretion on to massive black holes: the transition from radio AGN to quasars in brightest cluster galaxies. *Monthly Notices of the Royal Astronomical Society*, 432:530–553.
- Russell, H. R., Sanders, J. S., and Fabian, A. C. (2008). Direct X-ray spectral deprojection of galaxy clusters. *Monthly Notices of the Royal Astronomical Society*, 390(3):1207–1216.
- Sanders, J. S., Fabian, A. C., Russell, H. R., Walker, S. A., and Blundell, K. M. (2016a). Detecting edges in the X-ray surface brightness of galaxy clusters 1 2 3. *Monthly Notices of the Royal Astronomical Society*, 460(2):1898–1911.
- Sanders, J. S., Fabian, A. C., Taylor, G. B., Russell, H. R., Blundell, K. M., Canning, R. E. A., Walker, S. A., and Grimes, C. K. (2016b). A very deep Chandra view of metals, sloshing and feedback in the Centaurus cluster of galaxies. *Monthly Notices of the Royal Astronomical Society*, 457(1):82 – 109.
- Sarajedini, V. (2017). L3-ellipticals. University Lecture.
- Schlegel, E. M. (2002). *The Restless Universe: Understanding X-ray Astronomy in the Age of Chandra and Newton*. Oxford University Press, USA.
- Shen, J. and Gebhardt, K. (2009). The supermassive black hole and dark matter halo of NGC 4649 (M60). *Astrophysical Journal*.

- Shin, J., Woo, J.-H., and Mulchaey, J. S. (2016). A systematic search for X-ray cavities in galaxy clusters, groups, and elliptical galaxies. *The Astrophysical Journal Supplement Series*.
- Shurkin, K., Dunn, R. J. H., Gentile, G., Taylor, G. B., and Allen, S. W. (2008). Active galactic nuclei-induced cavities in NGC 1399 and NGC 4649. *Monthly Notices of the Royal Astronomical Society*, 383(3):923–930.
- Szegedy, C., Liu, W., Jia, Y., Sermanet, P., Reed, S., Anguelov, D., Erhan, D., Vanhoucke, V., and Rabinovich, A. (2014). Going Deeper with Convolutions. *arXiv:1409.4842*.
- Tonry, J. L., Dressler, A., Blakeslee, J. P., Ajhar, E. A., Fletcher, A. B., Luppino, G. A., Metzger, M. R., and Moore, C. B. (2001). The SBF Survey of Galaxy Distances. IV. SBF Magnitudes, Colors, and Distances. *The Astrophysical Journal*, 546(2):681–693.
- Tully, R. B., Courtois, H. M., Dolphin, A. E., Fisher, J. R., Héraudeau, P., Jacobs, B. A., Karachentsev, I. D., Makarov, D., Makarova, L., Mitronova, S., Rizzi, L., Shaya, E. J., Sorce, J. G., and Wu, P. F. (2013). Cosmicflows-2: The data. *Astronomical Journal*, 146(4).
- Walsh, J. L., Barth, A. J., and Sarzi, M. (2010). The supermassive black hole in M84 revisited. *The Astrophysical Journal*, 721(1):762–776.
- Weisskopf, M. C., Brinkman, B., Canizares, C., Garmire, G., Murray, S., and Van Speybroeck, L. P. (2002). An overview of the performance and scientific results from the Chandra X-Ray Observatory. *Publications of the Astronomical Society of the Pacific*, 114(791):1–24.
- Werner, N., Allen, S. W., and Simionescu, A. (2012). On the thermodynamic self-similarity of the nearest, most relaxed, giant ellipticals. *Monthly Notices of the Royal Astronomical Society*, 425(4):2731–2740.
- Wise, M. W., McNamara, B. R., Nulsen, P. E. J., Houck, J. C., and David, L. P. (2007). X-Ray Supercavities in the Hydra A Cluster and the Outburst History of the Central Galaxy’s Active Nucleus. *The Astrophysical Journal*, 659(2):1153–1158.
- Wood, R. A., Jones, C., Machacek, M. E., Forman, W. R., Bogdan, A., Andrade-Santos, F., Kraft, R. P., Paggi, A., and Roediger, E. (2017). The Infall of the Virgo Elliptical Galaxy M60 toward M87 and the Gaseous Structures Produced by Kelvin-Helmholtz Instabilities. *The Astrophysical Journal*, 847(1).
- Yan, M., Sadeghpour, R., and Dalgarno, A. (1998). Photoionization cross section of He and H₂. *The Astrophysical Journal*, 1(496):1044–1050.